Interannual and seasonal drivers of carbon cycle variability represented by the Community Earth System Model (CESM2)

W. R. Wieder[1,2*], Z. Butterfield[3], K. Lindsay[1], D. L. Lombardozzi[1], G. Keppel-Aleks[3]

[1] Climate and Global Dynamics Laboratory, National Center for Atmospheric Research, Boulder, CO 80307, USA.

[2] Institute of Arctic and Alpine Research, University of Colorado, Boulder, CO 80309, USA

[3] Department of Climate and Space Sciences and Engineering, University of Michigan, Ann Arbor, MI, 48109, USA

*Corresponding author: William Wieder (wwieder@ucar.edu)

Key Points

- Simulated net carbon fluxes show low interannual variability because of low tropical variability and high correlation in component fluxes
- Seasonal amplification and redistribution of fluxes characterize dominant modes of carbon cycle variability, consistent with observations
- Seasonal redistribution is characterized by warm springs, dry summers, and can result in a net carbon loss from land

Abstract

Earth system models are intended to make long-term projections, but they can be evaluated at interannual and seasonal time scales. Although the Community Earth System Model (CESM2) showed improvements in a number of terrestrial carbon cycle benchmarks, relative to its predecessor, our analysis suggests that the interannual variability (IAV) in net terrestrial carbon fluxes did not show similar improvements. The model simulated low IAV of net ecosystem production (NEP), resulting in a weaker than observed sensitivity of the carbon cycle to climate variability. Low IAV in net fluxes likely resulted from low variability in gross primary productivity (GPP)—especially in the tropics—and a high covariation between GPP and ecosystem respiration. Although lower than observed, the IAV of NEP had significant climate sensitivities, with positive NEP anomalies associated with warmer and drier conditions in high latitudes, and with wetter and cooler conditions in mid and low latitudes. We identified two

This is the author manuscript accepted for publication and has undergone full peer review but has not been through the copyediting, typesetting, pagination and proofreading process, which may lead to differences between this version and the Version of Record. Please cite this article as doi: 10.1029/2021GB007034.

dominant modes of seasonal variability in carbon cycle flux anomalies in our fully coupled CESM2 simulations that are characterized by seasonal amplification and redistribution of ecosystem fluxes. Seasonal amplification of net and gross carbon fluxes showed climate sensitivities mirroring those of annual fluxes. Seasonal redistribution of carbon fluxes is initiated by springtime temperature anomalies, but subsequently negative feedbacks in soil moisture during the summer and fall result in net annual carbon losses from land. These modes of variability are also seen in satellite proxies of GPP, suggesting that CESM2 appropriately represents regional sensitivities of photosynthesis to climate variability on seasonal time scales.

Plain Language Summary

Earth system models that are intended to make climate change projections also represent the global exchange of carbon dioxide (CO_2) between the atmosphere, oceans, and land. As such, the growth rate and variability of CO_2 concentrations in the atmosphere provide a robust measurement to evaluate models. We looked at the interannual variability of terrestrial carbon fluxes and their sensitivity to variations in temperature and water that were simulated by the Community Earth System Model (CESM2) and compared them to observations. We found that the model underestimates the interannual variability of net terrestrial carbon fluxes, especially in the tropics. We also identified two modes of variability that correspond to an increase in summer land carbon uptake (amplification) and a change in the seasonal timing (redistribution) of land carbon fluxes. Notably, seasonal redistribution was initialized by warmer springs that increased early-season productivity, but subsequent water limitations in the summer and fall resulted in lower-than-average productivity over the growing season and net annual C losses to the atmosphere. Similar patterns of seasonal amplification and redistribution are seen in satellite observations of photosynthesis, suggesting that the model is realistically simulating characteristics of terrestrial ecosystems necessary for capturing carbon cycle-climate feedbacks.

1. Introduction

Terrestrial ecosystems continue to provide a sink for about a quarter of anthropogenic carbon dioxide (CO_2) emissions (Ballantyne et al., 2012; Friedlingstein et al., 2019), but the long-term strength and locations of this sink remain uncertain (Gaubert et al., 2019; Schimel, Stephens & Fisher 2015; Tagesson et al., 2020). The net terrestrial flux of CO_2 to or from the atmosphere depends on the balance between much larger carbon fluxes that are driven by plant productivity, ecosystem respiration, and disturbances like fire (Keppel-Aleks et al., 2014). Observational constraints on these gross fluxes are difficult to make globally, which results in persistently high uncertainty in terrestrial carbon cycle projections (Anav et al., 2013; Arora et al., 2020; Friedlingstein et al., 2014, Liddicoat et al. 2021). Thus, capturing the appropriate carbon cycle sensitivities to climate driven variability at interannual and seasonal time scales over the observational record may be important to improving longer-term projections of terrestrial carbon balance.

At decadal- to century-time scales, the net exchange of CO_2 between the land and atmosphere remains one of the more robust benchmarks by which to evaluate the representation of terrestrial biogeochemistry in land models (Collier et al., 2018; Hoffman et al., 2014; Keppel-Aleks et al., 2013). Separately, the trends in the seasonal amplitude of terrestrial CO_2 fluxes provides insights to how global change drivers are altering the net exchange of terrestrial CO_2 with the atmosphere (Graven et al. 2013; Ito et al 2014; Piao et al. 2018). Indeed, successive generations of the Community Earth System Model (CESM) and its terrestrial component, the Community Land Model (CLM) show improvements in the globally integrated net terrestrial carbon flux over the historical period (Bonan et al., 2019; Danabasoglu et al., 2020; Lawrence et al., 2019). The model also shows improved seasonal amplitude of terrestrial CO_2 fluxes and better represents their increasing trend over the observational record (Lawrence et al. 2019; Lombardozzi et al. 2020). This suggests that the model adequately represents dominant features influencing longer-term trends in the terrestrial carbon cycle dynamics, namely land-use and land cover change as well as potential CO_2 fertilization effects (Wieder et al., 2019). These longer-term benchmarks, however, offer little insight into the environmental sensitivities of terrestrial CO_2 fluxes at annual to seasonal time scales, which are important for understanding carbon cycle sensitivities to climate variability and potential carbon cycle responses to future climate change.

Measurements of the atmospheric CO_2 growth rate provide an integrated estimate of the interannual variability (IAV) in global carbon cycle (Keeling et al., 1995; Zeng et al., 2005). Since much of the observed IAV is driven by terrestrial processes (Bousquet et al., 2000), variability in the atmospheric CO_2 record provides a top-town constraint on the climate sensitivity of land-atmospheric CO_2 exchange (reviewed by Piao et al., 2020). Specifically, natural climate variability in temperature and precipitation over land are the primary drivers of terrestrial carbon cycle variability that can be inferred from IAV in the atmospheric CO_2 growth rate. This includes the temperature sensitivity of gross primary productivity (GPP) and ecosystem respiration (R_{eco}) on net ecosystem exchange (NEE, calculated as GPP - R_{eco}), especially in the tropics (Anderegg et al., 2015; Ballantyne et al., 2017; Cox et al., 2013; Liu et al., 2017; Rödenbeck et al., 2018b; Wang et al., 2013). Meanwhile, other studies emphasize the importance of soil moisture variability on GPP and NEE, especially in arid and semi-arid ecosystems (Anderegg et al., 2015; Humphrey et al., 2018; Poulter et al., 2014). Jung et al. (2017) suggest that compensating moisture-driven variation in gross, local-scale fluxes (GPP and R_{eco}), as well as spatial compensation in moisture anomalies among regions leaves a dominant temperature-driven signal in the IAV of land-atmosphere CO_2 exchange. By using a mechanistic model we aim to provide simultaneous insights into the drivers of carbon cycle variability across a range of spatial scales, including finer spatial and temporal resolutions.

Disentangling the contributions of gross carbon fluxes and their impact on the IAV of NEE remains a challenge. While GPP and R_{eco} anomalies are strongly correlated, mounting evidence suggests that variance in NEE is more strongly correlated with variance in GPP than R_{eco} (Baldocchi et al., 2018; Schwalm et al., 2010). Globally gridded estimates of net and gross carbon fluxes are derived from upscaled flux tower measurements (Beer et al., 2010; Jung et al., 2011; Jung et al., 2017) or remote sensing (Alemohammad et al., 2017; Köhler et al., 2018; Running et al., 2004), but both of these tend to underestimate carbon cycle IAV (Jung et al., 2020; O'Sullivan et al., 2020; Piao et al., 2020; Y. Zhang et al., 2018). Remote sensing products offer promise for diagnosing seasonal productivity responses to climate variability in the tropics and extra-tropics (Bowman et al., 2017; Buermann et al., 2018; Li and Xiao, 2019; Liu et al., 2017; Schimel, Pavlick et al., 2015). Notably, Butterfield et al. (2020) found that while local to regional-scale IAV in productivity was poorly correlated among remote sensing products (between 2007-2015), they could identify seasonal modes of variability that shared common

features and environmental sensitivities. These included the: 1) Amplification of the seasonal cycle of GPP, which was associated with increases in summertime soil moisture availability and positive anomalies in GPP, and 2) Seasonal redistribution of GPP that was initially driven by warmer springtime temperatures—resulting in positive GPP anomalies—but that was followed by higher-than-average soil moisture stress in the summer and fall—resulting in negative GPP anomalies (see also Byrne et al. 2020). Integrated over the growing season, the second mode of variability reflects climate driven shifts in the seasonal timing of photosynthesis, which has negligible changes in the annual C flux.

Given improvements to the representation of terrestrial biogeochemistry in CESM2, relative to CESM1 (Bonan et al. 2019; Danabasoglu et al., 2020; Lawrence et al. 2019; Lombardozzi et al. 2020), we investigated the representation of carbon cycle variability at interannual and seasonal timescales in the model. Part of this work was motivated by findings of Lawrence et al. (2019), who noted that metrics for terrestrial carbon cycle interannual variability were degraded in CLM5, especially in the tropics, relative to previous versions of the model. Second, given new observational analysis that identified dominant modes of seasonal variability in regional productivity over the satellite record (Butterfield et al. 2020; Byrne et al. 2020) we explored the predictive model's ability to simulate similar behavior in global-scale simulations. Thus, our aims were to: 1) Quantify the IAV of land carbon fluxes simulated over the historical period by CESM2-esm-hist and their sensitivity to climate variability; 2) Identify modes of seasonal variability in simulated carbon fluxes and their likely climate drivers.

2. Methods

2.1 Model simulations

We analyzed simulations from the Community Earth System Model, version 2 (CESM2) that couples atmosphere, ocean, land, sea ice, land ice, and river transport components to simulate physical and biogeochemical conditions over historical and future scenarios (Danabasoglu et al., 2020). Of greatest importance for the simulations analyzed here are the atmospheric and land components, which are each briefly described below. The atmosphere model in CESM2 is the Community Atmosphere Model, version 6 (CAM6) which applies the same Finite Volume dynamical core (Danabasoglu et al., 2020). Relative to previous versions of the model, CESM2 shows an improvement in its representation of El Niño Southern Oscillation (ENSO) events and their effect on precipitation and temperature anomaly patterns (Meehl et al., 2020). The

atmosphere and land models are run at a nominal 1° horizontal resolution (1.25° longitude by 0.9° latitude) and are coupled every 30 minutes.

The terrestrial component of CESM2 uses the Community Land Model, version 5 (CLM5; Lawrence et al., 2019). Briefly, these developments simulate transient agricultural expansion and land management (Lombardozzi et al., 2020), plant hydraulic stress (Kennedy et al., 2019), and improve the representation of plant nitrogen limitation (R. A. Fisher et al., 2019; Wieder et al., 2019). We used the historical simulation of CESM2-esm-hist from 1850-2014 that has active biogeochemical representation of terrestrial carbon and nitrogen cycles and that also simulates the prognostic evolution of atmospheric CO_2 concentrations based on fluxes with oceans and terrestrial ecosystems.

As described in Danabasoglu et al. (2020), initial conditions for the land model and ocean model biogeochemical tracers in the non-ESM piControl experiment were generated using spin-up runs of the land and ocean models, respectively. In these spin-up runs, the active atmospheric component was replaced with a data atmosphere that repeatedly cycled through twenty-one years of surface forcing that were extracted from a fully coupled CESM2 experiment. Twenty-one years of forcing were used to capture some aspects of interannual variability. The land model spin-up consisted of an accelerated decomposition (AD) mode segment and a subsequent synchronous spin-up segment. These segments were run for 252 and 1701 years respectively. The ocean model spin-up was applied to biogeochemical tracers. The ocean spin-up was run for 1029 years and also utilized a Newton-Krylov solver, based on Lindsay (2017) to more completely spin up a subset of the biogeochemical tracers, including the carbon pools. The esm-piControl was initialized from the piControl experiment using an incremental coupling approach. In an intermediate experiment, which was initialized from the piControl experiment, the carbon cycle of the surface components was coupled bidirectionally to a CO_2 tracer in the atmospheric model. This intermediate experiment was run for 80 years, during which the surface biogeochemical parameterizations adjusted to the prognostic atmospheric CO_2. The esm-piControl experiment was initialized with the model state from the end of this intermediate experiment, and the prognostic CO_2 was coupled to the radiative computations in the atmospheric model. The esm-hist experiments analyzed here were initialized from the esm-piControl experiment. The CESM2-esm historical simulations used CMIP6 forcings for anthropogenic emissions, biomass burning, and volcanic SO_2 emissions from 1850-2014

described in Danabasoglu et al. (2020) as well as land use and land cover change described in Lawrence et al. (2019) following CMIP6 protocols outlined by Eyring et al. (2016).

Using a single ensemble member of CESM2-esm-hist, we focused our analysis on carbon fluxes that are simulated during the end of the historical period (1960-2014), which overlaps with atmospheric CO_2 measurements. We quantified variability in carbon fluxes at interannual and seasonal time scales and correlated these fluxes with anomalies in climate drivers (temperature and moisture). The model simulates gross fluxes of GPP and R_{eco}, with the difference between them representing net ecosystem production (NEP). Positive values for NEP represent net terrestrial ecosystem uptake of carbon. We focused on NEP instead of net ecosystem exchange or net biome production (NEE and NBP, respectively), which include fluxes from fire, land use, and land management, because the CESM2-esm-hist simulations have unrealistically large fire carbon fluxes from land degradation in the tropics at the end of the historical period.

2.2 Statistical Analyses

2.2.1: Interannual variability

We summed monthly carbon fluxes (NEP, GPP, and R_{eco}) that were simulated from vegetated terrestrial grid cells to calculate accumulated annual fluxes and weighted them by grid cell area and land fraction to calculate global values. We similarly calculated mean annual temperature (TBOT) and terrestrial water storage (TWS) that was simulated by the model. The CESM2-esm results showed strong long-term trends in relevant variables (Fig. S1), so we subtracted linear trends and focused on the detrended anomalies from the climatological mean state for both monthly and annual data.

The IAV was calculated as the standard deviation of annual results simulated from 1960-2014. We compared the IAV in global detrended anomalies of simulated CO_2 fluxes, simulated land CO_2 fluxes, and NEP to those observed in the atmospheric CO_2 growth rate reported by the Global Carbon Project (Friedlingstein et al., 2019). As most of the variability in global CO_2 fluxes is driven by IAV in terrestrial fluxes (Fig. S2), we focus on the IAV of NEP and its component fluxes.

Lagged correlations reveal teleconnections between modes of climate variability, like ENSO, that are associated with atmospheric CO_2 anomalies and terrestrial CO_2 fluxes (Braswell et al 1997, see also Lindsay et al. 2014). Ecosystems, however, are responding to local climate

conditions, where Bloom et al (2020) also inferred significant ecosystem carbon cycle memory from lagged correlations with local climate anomalies. While both lagged responses are important features of terrestrial ecosystem response to climate variability, we focus here on documenting the immediate, lag-zero response of fluxes simulated by CESM2-esm. To characterize relationships in the data we calculated Pearson's correlation coefficients and regression statistics between detrended anomalies in carbon fluxes, moisture, and temperature. We also calculated the grid cell variance and standard deviation of annual, detrended carbon fluxes to look at covariation between simulated fluxes (as in Baldocchi et al., 2018).

2.2.2: Seasonal modes of interannual variability

To decompose the annual cycle of carbon fluxes simulated in each terrestrial grid cell and identify modes of variability we used a singular value decomposition (SVD; Golub & Reinsch, 1971 as in Butterfield et al., 2020). The SVD decomposed the time series of detrended flux anomalies into singular vectors (SV_i), the elements of which reflect the month (m) of the year (y; Fig. S3). Vectors are ranked by the fraction of variance they explain in the time series. Each singular vector also receives a weight w_i, one per year per singular vector, that quantifies the contribution from an individual singular vector to the observed IAV in any given year. Thus, the simulated IAV time series for a grid cell can be fully reconstructed as the weighted sum of singular vectors:

$$\mathbf{IAV}(y,m) = \Sigma_i\, w_i(y) \times \mathbf{SV}_{\boldsymbol{i}}(m) \qquad (1)$$

Our SVD had 55 singular vectors (*i*, corresponding to the number of years in our analysis). Given recent publications that use and SVD to characterize seasonal variability in regional GPP fluxes (Butterfield et al. 2020; Byrne et al. 2020) we evaluated the model GPP using the same approach, but extend the analysis to also include grid-cell variation in NEP simulated by CESM2-esm, using the first two singular vectors to characterize the dominant modes of variability. We also calculated a redistribution metric, $\boldsymbol{\theta}$, as the sum of elements from a singular vector divided by the absolute values of the sum of elements from that vector (Butterfield et al. 2020).

$$\boldsymbol{\theta} = \Sigma_m\, \mathbf{SV}_i(m) \,/\, \Sigma_m\, |\mathbf{SV}_i(m)| \qquad (2)$$

Thus, when $\boldsymbol{\theta} = 0$, NEP was redistributed within the growing season without changing the annual flux. By contrast, values of $\boldsymbol{\theta} = 1$ (or -1) indicate that every month had a positive (or negative) anomaly in GPP relative to the multi-year mean.

We identified the mode of variability corresponding to a seasonal amplification of NEP as the vector whose elements most strongly correlated with annual climatology of NEP. At annual time scales, the amplification vector corresponds to a net increase (or decrease) in terrestrial NEP, compared to the monthly detrended climatological mean. The other mode of variability corresponded to a seasonal redistribution of NEP, which typically has both positive and negative phases. In the northern hemisphere, this typically results from anomalously high plant productivity in the spring that is followed by lower-than-average plant productivity in the summer and fall (Fig. S4 and results in section 3.2; see also Butterfield et al. 2020). Thus, the redistribution vector does not necessarily result in a change in the net annual carbon flux, but it indicates changes in the seasonal timing of ecosystem production, relative to the monthly detrended climatological mean.

The $\boldsymbol{\theta}$ values were used to confirm the appropriate identification of amplification and redistribution modes of variability in each grid cell (e.g., $|\boldsymbol{\theta}|_{\text{amplification}} > |\boldsymbol{\theta}|_{\text{redistribution}}$). To facilitate our analysis, we reversed the sign of singular vector elements, weights and $\boldsymbol{\theta}$ values so that amplification vectors were positively correlated with the annual climatology of carbon fluxes and the redistribution vector started with a positive phase (Fig. S4). For visualization we calculated regional means for elements in the seasonal amplification and redistribution vectors across high, mid, and low latitude bands in both hemispheres (50-80°, 20-50°, and 0-20°, respectively). Finally, to link modes of carbon cycle variability back to climate anomalies we calculated seasonal means for NEP, air temperature, and terrestrial water storage anomalies. We looked at Pearson's correlation coefficients between these seasonal anomalies and the SVD weights generated for amplification and redistribution vectors.

3 Results

3.1 Interannual variability

Detrended anomalies of terrestrial net ecosystem production (NEP) that are simulated by CESM2-esm have low variability, compared to the atmospheric growth rate of CO_2 measured since 1959 and reported by the Global Carbon Project (Friedlingstein et al., 2019; Figs. 1a, S2). The standard deviation of modeled NEP fluxes (0.47 Pg C y^{-1}) is roughly half of the standard

deviation in the observed atmospheric CO_2 growth rate (0.95 Pg C y^{-1}; Friedlingstein et al., 2019; Rödenbeck et al., 2018a). Notably, the standard deviation of annual detrended NEP fluxes in the tropics (23°S-23°N) simulated by CESM2-esm is 0.24 Pg C y^{-1}, roughly a factor of three lower than estimates from inversion models over land (90°S-25°N, 0.6-0.8 Pg C y^{-1}; Rödenbeck et al., 2018a). Note, for convenience we inverted the sign of the atmospheric growth rate so that positive anomalies in Fig. 1a show net land C uptake for both the model and observations. We also note that any temporal correlations between C flux anomalies in CESM2-esm simulations and atmospheric observations here are unintended, because CESM2-esm is experiencing a modeled atmosphere that does not necessarily match local, regional, or global conditions experienced during the historical record of atmospheric CO_2 observations. The low IAV of net terrestrial C exchange with the atmosphere in CESM-esm could be driven by a number of factors that include low climate variability in the coupled model, low sensitivity of component fluxes (GPP and R_{eco}) to climate variability, or high correlation between component fluxes at annual timescales that results in a dampening of IAV in the net carbon flux.

To investigate the hypothesis that the low IAV of net terrestrial C exchange could be caused by low climate variability in in the coupled model, we plot in Fig. 1b the detrended annual anomalies of NEP (as in Fig. 1a) along with annual anomalies in terrestrial water storage (over vegetated grid cells) and tropical air temperatures over land (23°S - 23°N). The magnitude of terrestrial water storage and tropical air temperature variability simulated in CESM2-esm seems reasonable, compared to observations (σ = 0.82 Tt H_2O and 0.10 K, respectively; Fig. 1b; Cox et al., 2013; Humphrey et al., 2018). Consistent with the low carbon cycle variability simulated by CESM2-esm (Fig. 1a-b), however, the model shows weaker than observed carbon-cycle sensitivity to global and regional climate anomalies (Fig. 1c-d). The anomalies between NEP and terrestrial water storage are statistically significant (r = 0.63, p<0.001), but with a weaker than observed effect on carbon cycle variability (slope = 0.36 Pg C y^{-1} Tt H_2O^{-1} vs. r = 0.85, slope = 1.3 Pg C y^{-1} Tt H_2O^{-1} in Humphrey et al., 2018). We similarly find significant correlations between simulated anomalies of NEP and tropical temperature (r = -0.58, p<0.001, slope = -2.6 Pg C y^{-1} K^{-1}), but this relationship is also weaker than observed estimates [Cox et al. (2013), r = -0.65, slope = -5.1 Pg C y^{-1} K^{-1}; Wang et al. (2013), r = -0.7, slope = -3.5 Pg C y^{-1} K^{-1}] (see also Fig S5, Ballantyne et al., 2017; Rödenbeck et al., 2018a). Supplementary Fig. S5 shows that when forced with historical climate reanalysis land-only simulations with CLM5 (Lawrence et

al. 2019) capture the appropriate sign of terrestrial carbon cycle IAV observed in the atmospheric record, but not an appropriate magnitude of response, especially to the 1986-87 or 1997-98 El Niño events, resulting in low IAV of NEP fluxes (σ = 0.41 Pg C y^{-1}). These land-only simulations show similar IAV of terrestrial water storage and tropical air temperatures as results from the coupled model (σ = 0.80 Tt H_2O and 0.07 K, respectively), suggesting that the CESM2-esm adequately represents climate variability over terrestrial ecosystems.

Observed and simulated variability in NEP is driven by variability in component fluxes, gross primary productivity (GPP) and ecosystem respiration (R_{eco}). The global mean IAV of detrended GPP and R_{eco} anomalies were 1.4 and 1.1 Pg C y^{-1}, respectively. These values for GPP are in line with those reported by Chen et al. (2017) who looked at the IAV of GPP from ensemble of land models and upscaled flux tower estimates (1.4 and 1.5 Pg C y^{-1}, respectively). Elsewhere, O'Sullivan et al. (2020) found little agreement in the magnitude of IAV of GPP simulated by different ensemble of land models (which included CLM4.5), upscaled flux tower observations, and remote sensing derived light-use efficiency models, especially in highly productive tropical forests. This highlights the challenge in assessing global scale variability in plant productivity without direct observations. The challenges are even greater for ecosystem respiration, which has no remote sensing proxy and can only be indirectly inferred as the residual of other component fluxes, which are themselves highly uncertain (Basile et al. 2020; Chevallier, 2018; Liu et al., 2017).

Disaggregating the global fluxes simulated by CESM2-esm into their gridcell contributions provides another perspective on component fluxes simulated by the model. The mean standard deviation of detrended GPP and R_{eco} anomalies (102 and 83.8 g C m^{-2} y^{-1}, respectively) in CESM2 were about 10% of the mean fluxes (950 and 910 g C m^{-2} y^{-1}, respectively). Again, these estimates of GPP IAV agree with those reported from an ensemble of land models (96 g C m^{-2} y^{-1}; O'Sullivan et al. 2020), but we note that the ensemble of prognostic models generally simulate lower IAV than FLUXCOM estimates and light-use efficiency models (see also Jung et al., 2017). CESM2-esm shows high IAV of detrended GPP fluxes in tropical savannah regions, but relatively low coefficient of variation in humid tropical forests (Fig. S6). This feature is commonly seen in land models (O'Sullivan et al. 2020) and is inconsistent with observations from tropical forests (Bowman et al., 2017; Liu et al., 2017). Thus, we see the low IAV in

simulated GPP fluxes as a major limitation in current land models, including CLM5, and note this as a priority area for future model developments.

Outside of the tropics, we compared the coefficients of variability (defined as the ratio of the interannual standard deviations to the seasonal amplitude of the multi-year mean) in four ecoregions of North America as defined in Butterfield et al. (2020) from CESM2 and several remote sensing products (Table S1). The various remote sensing products show a factor of two difference in the range of variability in regional GPP estimates, and the magnitude of GPP variability simulated by CESM2 is comparable to these observationally derived estimates. This finding contradicts results reported by Wozniak et al. (2020), who found lower than observed variability in land-only simulations conducted with CLM5 at flux tower sites.

Grid cell variance of NEP was strongly and positively correlated with the variance of component fluxes (Fig. 2a). Although variance in NEP is slightly better explained by GPP variance ($r = 0.79$, slope = 0.77) than R_{eco} variance ($r = 0.74$, slope = 0.72; Fig. 2a), the anomalies of the component fluxes are highly correlated with each other ($r = 0.94$, slope = 0.80; Fig. 2b). By contrast, observations from FLUXNET show lower correlations between GPP and R_{eco} anomalies ($r = 0.70$, slope = 0.42; Baldocchi et al. 2018). We acknowledge that estimates of GPP and R_{eco} from flux tower observations are a modeled product derived from NEE measurements. Moreover, these measurements are biased towards to relatively mesic temperature environments, creating a scale mismatch when used to evaluate results from a global model (Pastorello et al., 2017; Schimel, Pavlick et al., 2015). Regardless, the strong simulated correlation between simulated GPP and R_{eco} likely accounts for some of the low interannual variability in land carbon uptake in CESM2-esm, since years with large GPP fluxes are necessarily compensated by R_{eco} fluxes that are of nearly the same magnitude.

Numerous developments went into CLM5 (described in Lawrence et al. 2019), but we briefly explore the underlying causes for the high correlation between GPP and R_{eco} fluxes in the model that are shown in Figure 2. The components of R_{eco} include autotrophic and heterotrophic respiration. We found that annual gridcell R_{eco} anomalies were most strongly correlated with annual anomalies in autotrophic respiration fluxes (Fig S7a). The components of autotrophic respiration include growth respiration, maintenance respiration, and a new plant respiration flux that is associated with the fixation and uptake of nitrogen model (FUN; R. A. Fisher et al., 2019; Shi et al., 2016). Of these, we find that anomalies associated with FUN are most strongly

correlated with the autotrophic respiration fluxes simulated by CESM2-esm (Fig. S7b). From a mechanistic perspective, this high correlation makes sense, since for each additional increment in GPP, a corresponding increment in respiration is required to meet associated nitrogen demand associated with plant growth. This flux, however, occurs instantaneously in CLM5, and thus dampens potential IAV of net fluxes. In real ecosystems there is longer lag between photosynthesis and autotrophic respiration fluxes, notably those associated with plant nutrient uptake. Measuring and modeling these fluxes, especially related to non-structural carbohydrates (Martínez-Vilalta, et al 2016) remains an outstanding challenge.

The IAV of detrended NEP anomalies simulated in CESM2-esm is positively correlated with terrestrial water storage anomalies in low and mid latitude regions (50°S - 50°N), whereas high latitude ecosystems show a negative correlation between NEP and water storage anomalies (Fig. 3a). These patterns are reversed for correlations between NEP and air temperature anomalies (Fig. 3b). Over cold regions, and especially in boreal forests, the IAV of detrended NEP anomalies are positively correlated with air temperature anomalies. By contrast, over mid and low latitudes, especially in the Amazon, SE Asia, and N Australia, the IAV of detrended NEP anomalies are negatively correlated with air temperature anomalies. At annual time scales NEP anomalies show stronger correlations with GPP anomalies than they do with ecosystem respiration anomalies (Fig. 3c-d). Figure S8 shows correlations of annual GPP, total water storage, and temperature anomalies.

3.2 Seasonal variability

The first two vectors in the singular value decomposition explained 68% (area weighted mean) of the variance in NEP over the vegetated land surface. In general, the amplification vector explained the greatest fraction of variance in NEP, especially in arctic and boreal regions, as well as arid and temperate regions like the western North America (global area weighted mean = 39%; Fig. 4a). The redistribution vector explained the largest fraction of variation over more mesic regions in the mid latitudes, especially temperate deciduous forest and agricultural regions in the eastern North America and Europe (global weighted mean = 29%; Fig. 4b). Neither vector explained a large fraction of NEP variance over tropical forests, which generally showed low variability in detrended GPP anomalies (Fig. S6). Figure S9 shows SVD results for GPP, which explained 75% for the total variance in GPP (45% and 29%, for amplification and redistribution

vectors, respectively). The modes of variability simulated by CESM2-esm with amplification and redistribution in western and eastern United States, respectively, are qualitatively similar to patterns observed in remote sensing estimates of GPP and flux inversions of NEE (Byrne et al. 2020).

Figure 5 shows the mean annual climatology of the NEP, as well as the monthly values for amplification and redistribution vectors (grey, blue, and red lines respectively) for latitudinal bins. High and mid latitudes are characterized by a distinct annual cycle of NEP that is strongly correlated with the amplification vectors describing NEP variability (Fig. 5a, b, d). The amplification vector describes 48%, 40%, and 32% of the NEP variability in arctic, northern hemisphere temperate, and southern hemisphere temperate latitudinal zones, respectively. By contrast, the redistribution vectors in these regions explain 26-28% of the NEP variability and are characterized by positive spring-time anomalies that are followed by negative NEP anomalies in the summer and fall, relative to the monthly climatology. In the tropics, the seasonal cycle is more muted, but seasonal amplification and redistribution vectors describe roughly 35% and 28% of the variability in NEP, respectively (Fig. 5c, e). Figure 6 shows analogous plots for the mean monthly vectors for the SVD of GPP anomalies, which illustrates modes of seasonal variability in GPP that are simulated by CESM2-esm are similar to those reported from remote sensing observations (Butterfield et al., 2020; Byrne et al., 2020).

The θ values calculated in the SVD show the net impact on the integrated seasonal signal of NEP. The mean θ values associated with the amplification vector are globally positive (Fig. 5). By contrast, the θ values associated with a seasonal redistribution of NEP are negative, or close to zero. This indicates that a negative, or little change in integrated seasonal signal of net carbon fluxes from seasonal redistribution of NEP. The redistribution vectors of GPP anomalies largely have θ values close to zero (Fig. 6). Notably, redistribution of GPP in temperate and boreal regions leads to no net change in the annual uptake of CO_2 (Fig. 6). Net fluxes, however, in high latitude ecosystems show an annually integrated loss of C from land to the atmosphere with seasonal redistribution of fluxes ($\theta < 0$, Fig. 5a). These dynamics are driven by concurrent, higher than average (positive) spring anomalies in heterotrophic respiration fluxes (Fig. S10) that cancel positive anomalies in GPP, resulting in negligible net C uptake in the spring (Fig. 5a).

More broadly, although the seasonal redistribution of carbon variability is a major source of global carbon cycle variability in the model, it would not be evident in more aggregated metrics of variability that only look at annual times-scales (e.g., Figs. 1, S5).

To evaluate the environmental drivers of carbon cycle variability we conducted linear regressions on the weights of the amplification (Fig. 7) and redistribution (Fig. 8) vectors from SVD analysis (n = 55, for each year of the simulation) with seasonal anomalies of carbon fluxes, terrestrial water storage, and air temperature. We focus our analysis on GPP to isolate between the environmental sensitivities of component fluxes of NEP. The SVD weights for the amplification vector of GPP were strongly and positively correlated with the GPP anomalies during the peak of the growing season (Fig. 7, left column). This is expected, since the amplification vector was identified by its correlations with the climatology of GPP. As such, correlation coefficients are highest in the summer months (JJA and DJF for northern and southern hemispheres, respectively). Strong correlations are evident at other times (e.g., negative correlations between weights and GPP anomalies across high latitudes in DJF), but the magnitude of these anomalies is small relative to the annual cycle (see also Fig. 6a). Although terrestrial water storage and air temperature covary (Fig. S8c), high-latitude ecosystems generally show SVD amplification weights that are more positively correlated with air temperature anomalies and negatively correlated with water storage anomalies in JJA (Fig. 7, right and middle columns, Table S2). By contrast, across mid and low latitudes, SVD amplification weights for GPP are more strongly and positively correlated with wetter-than-average conditions and negatively correlated with air temperature anomalies.

The SVD weights for the redistribution vector were strongly and positively correlated with the GPP anomalies during the spring, with correlation coefficients that are highest in the MAM and SON (for northern and southern hemispheres, respectively; Fig. 8, left column). In the northern hemisphere, the positive phase of the redistribution vector is also more strongly correlated with warmer spring-time air temperatures (Fig. 8, right column) than terrestrial water storage. Subsequent GPP anomalies in the summer and fall, however, show negative correlations with SVD weights (see also Fig. 6). The summer (JJA) is still characterized by warmer, but also drier-than-average conditions (Fig. 8, middle column; Table S3) that also have negative GPP anomalies. By fall (SON), these negative GPP anomalies are only associated with drier-than-average conditions. Thus, the positive phase of the redistribution vector associated with warmer-

than-average springs is (nearly) canceled by the subsequent soil moisture stress and lower-than-average productivity in the summer and fall, resulting in minimal change in annual productivity.

4. Discussion

4.1 Interannual variability

Our results show that the magnitude of global carbon cycle interannual variability simulated by CESM2-esm is low, relative to measurements of IAV in the atmospheric CO_2 growth rate (Fig. 1). The CESM2 has a good representation of precipitation and temperature anomaly patterns associated with tropical Pacific sea surface temperatures (Danabasoglu et al., 2020; Meehl et al., 2020). Accordingly, the magnitude of terrestrial water storage and air temperature variability agrees reasonably well with observations (Fig. 1; Cox et al., 2013; Humphrey et al., 2018). This suggests that the model adequately represents global-scale climate variability, but that this climate variability does not generate enough terrestrial carbon cycle variability in the model.

Because the timing of moisture or temperature variability in the coupled model are not expected to agree with the timing of these variations in the historical, observational record, we instead analyze relationships between carbon fluxes and climate anomalies. The model shows lower than observed sensitivity of net C fluxes to climate variability in moisture and temperature anomalies (Fig. 1c, d; Cox et al 2013; Humphrey et al. 2017; Wang et al. 2013). We appreciate that these studies all use slightly different time periods for their calculations, but we do not expect this to significantly alter the fundamental sensitivities of land carbon fluxes to climate variability. Including terrestrial CO_2 fluxes associated with land use change and fire does not meaningfully change the magnitude of IAV of net carbon fluxes that are simulated by the model (Fig. S2; excluding the year 2010). The finding that simulated C fluxes in the coupled model have low IAV is generally consistent with land-only CLM5 simulations, which also shows weaker than observed carbon cycle variability when driven by reanalysis climate forcing data that reflects the historical drivers of the observed carbon cycle variations (Fig. S5), even when including C fluxes associated with land use change and fires (Lawrence et al., 2019). Notably, these offline simulations capture the sign of terrestrial carbon cycle IAV observed in the atmospheric record, the model does not simulate the appropriate magnitude of response to the 1986-87 or 1997-98 El Niño events.

The IAV in net carbon fluxes results from variability in component fluxes (GPP and R_{eco}) and their interaction (Baldocchi et al., 2018; Lasslop et al., 2010). Simulations from CESM2-esm show strong correlations between NEP and both of its component fluxes (Fig. 2a). Our results suggest that CESM2-esm shows notably low IAV of GPP fluxes in tropical forests (Fig. S6). This feature of the terrestrial C cycle simulated by CESM2-esm (and CLM5) is not consistent with observations that suggest tropical forests respond strongly to variability in the climate system (Bastos et al., 2018; Cavaleri et al., 2017; Liu et al., 2017; Rödenbeck et al., 2018a). Ensembles of land models typically do a good job of matching the IAV of the atmospheric growth rate (Ahlström et al., 2015; Friedlingstein et al., 2019; Poulter et al., 2014), but O'Sullivan et al. (2020) recently found that land models, including CLM4.5, generally simulate low IAV of GPP fluxes in tropical forests. This suggests broader deficiencies in land models' ability to capture appropriate mechanisms for C cycle IAV, which are also evident in our CESM2-esm simulations. Future work, therefore, should focus on understanding and improving the simulation of gross and net carbon cycle sensitivities to climate variability, especially in the humid tropics. Notably uncertainties in tropical forest IAV are related to how models like CLM simulate phenology, as well as temperature and moisture stress on photosynthesis and stomatal conductance. Indeed, O'Sullivan et al (2020) emphasize this broader challenge in understanding the magnitude and drivers of tropical forest variability in models and observations.

Low variability in plant productivity simulated by CESM-esm may extend beyond the tropics. For example, Wozniak et al. (2020) found that maximum rates of GPP simulated by CLM in temperate deciduous forests were much lower than observations at a number of AmeriFlux sites. Indeed, measurements from flux towers suggest that brief periods of large photosynthetic uptake appear to be an important component of the IAV in net carbon exchange, especially in arid ecosystems (Fu et al., 2019; Kannenberg et al., 2020; Zscheischler et al., 2016). The failure of CLM5 to simulate high rates of GPP during favorable conditions suggests that the model needs parametric or structural changes in its representation of leaf-level photosynthesis, stomatal conductance, or canopy scaling to represent photosynthetic variability. Regional analyses comparing the IAV of GPP in CESM-esm simulations to remote sensing estimates suggest that the variation in GPP fluxes may be appropriate for four regions of North America (Table S1; Butterfield et al., 2020). Additional work is, however, needed to evaluate the feasibility of quantifying IAV of carbon cycle components from remote sensing products

(Bowman et al., 2017; Liu et al., 2017; Schimel, Pavlick et al., 2015) and comparing the result to Earth system models, especially in the tropics.

Observations suggest that site-level variance in net carbon fluxes is more tightly correlated with GPP than R_{eco} (Baldocchi et al., 2018), which is also true in our simulations (Fig. 3c-d). Broadly, we note that models like CLM tends to overestimate respiration fluxes because they do not simulate other ecosystem C losses pathways that may have longer residence times (Randerson et al., 2002; Trumbore, 2006; Ciais et al, 2020). The anomalies of GPP and R_{eco} that are simulated by CESM2-esm are more strongly correlated than observations suggest (Fig 2b, Baldocchi et al., 2018). This high covariation between GPP and R_{eco} offsets variance in either of the component fluxes and dampens the IAV of NEP in the model. These results also suggest that the current structure and parameterization of CESM2-esm, which dictates the high covariance of simulated GPP and R_{eco}, should be revised (although evaluating R_{eco} fluxes is challenging without spatiotemporally explicit estimates for model benchmarking). We suspect that several changes made to the land model for CESM2 have exacerbated this problem.

First, CLM5 reduced the magnitude of growth respiration fluxes (Atkin et al., 2017) and reduced the total C fluxes associated with growth and maintenance respiration fluxes, relative to previous versions of the model (Lawrence et al., 2019). Second, the incorporation of the Fixation and Uptake of Nitrogen model (FUN) into CLM5 makes plants pay the carbon costs of nitrogen uptake (J. B. Fisher et al., 2010; R. A. Fisher et al., 2019; Shi et al., 2016). As currently applied in CLM5, the anomalies in FUN carbon costs are highly correlated with autotrophic respiration and, by extension, NEP anomalies (Fig. S7). This follows the logic currently built into the model, whereby plants instantaneously allocate new photosynthate to build biomass or meet respiration demands and remaining carbon is used for nitrogen acquisition by FUN. In real ecosystems this expenditure of carbon to acquire nitrogen would occur below ground, with at least some of the carbon interacting with the soil matrix (e.g., through root exudates). Moreover, this transfer of fresh photosynthate belowground for nitrogen uptake does not occur instantaneously, as it does in the model. Future developments should address these deficiencies in CLM5. Finally, the parameterization for soil organic matter turnover uses a higher minimum water potential, which increases the sensitivity of heterotrophic respiration fluxes to liquid soil water availability (Carvalhais et al., 2014; Koven et al., 2017; Lawrence et al., 2019; Z. Liu et al., 2018). Independently, these changes to growth respiration, FUN, and heterotrophic respiration fluxes

seem justified in their aim to represent terrestrial ecosystems more realistically, but together they likely served to reduce the IAV of net carbon fluxes that are simulated by CESM2-esm.

The correlations of NEP and GPP anomalies with climate drivers in CESM2-esm show strong latitudinal patterns (Figs. 3, S8). Notably, correlations between carbon flux and terrestrial water storage anomalies are particularly strong in many arid, semi-arid and savannah regions (Figs. 3a, S8a), a finding that is consistent with work emphasizing moisture and precipitation controls over carbon cycle variability in arid regions (Ahlström et al., 2015; Humphrey et al., 2018; Poulter et al., 2014). Concurrently, correlations between carbon flux and air temperature anomalies are stronger in arctic, boreal and temperate deciduous forests (Figs. 3b, S8b), which again is consistent with observations (discussed in section 4.2; Hu et al., 2019; Rödenbeck et al., 2018b). We recognize that inferring the relative importance of climate controls over land-atmosphere carbon exchange remain actively discussed in the literature (Cox et al., 2013; Humphrey et al., 2018; Jung et al., 2017; Piao et al., 2020; Poulter et al., 2014). Given the spatial and temporal heterogeneity of climate anomalies and timescales of ecosystem responses (Rödenbeck et al., 2018b; X. Zhang et al., 2013) we investigated the seasonal modes of carbon cycle variability that are simulated by CESM2-esm and their environmental covariates.

4.2 Seasonal variability

The timing of climate variations with respect to the climatological annual cycle plays an important role in the resulting seasonal and interannual variability of terrestrial carbon fluxes (Buermann et al., 2018). Satellite and flux tower observations in North America suggest that carbon cycle variability can be decomposed into modes of variability that are characterized by the amplification and redistribution of seasonal fluxes (Butterfield et al., 2020; Byrne et al., 2020). Likewise, the SVD analysis identified similar modes of variability in NEP and GPP simulated in CESM2-esm (Figs. 4, S9). Amplification vectors are dominant in high latitude and arid ecosystems, while redistribution vectors that are dominant in temperate forests, boreal forests, and agricultural regions. Qualitatively, these patterns align with findings from (Butterfield et al., 2020) who found robust patterns in seasonal GPP variability from several satellite datasets that are correlated with regional anomalies of temperature and soil moisture availability. The similarity in spatial patterns of NEP and GPP variability form our SVD analyses illustrate the strong dependence of modeled NEP variability on GPP, but we recognize that

seasonal changes in ecosystem respiration that are also important drivers of carbon cycle variability (Basile et al., 2020; Commane et al., 2017; J. Liu et al., 2017; Z. Liu et al., 2018; Welp et al. 2007).

In grid cells where the seasonal amplification of carbon cycle fluxes characterizes most of the flux variability the second vector from the SVD corresponds to a seasonal redistribution of the fluxes (Figs. 4-6). For example, in high latitude ecosystems the amplification vector describes nearly half of the variability in simulated NEP and is associated with a net increase (or decrease) in annual carbon fluxes (Fig. 5a). The weights associated with the amplification vectors are most strongly correlated with summertime GPP anomalies (Fig. 7, top row; Table S2), which is not surprising since we identified the amplification vector from the SVD by its correlation with the mean climatology of monthly fluxes simulated in each grid cell (section 2.2; Fig. S4). The weights from the amplification vectors in high latitude ecosystems also show a strong, positive correlation with summertime air temperature anomalies and a weaker, but still significant, negative correlation with terrestrial water storage anomalies. Thus, with warmer (and drier) summertime conditions, CESM2-esm simulated positive GPP anomalies in arctic and boreal ecosystems. Conversely, with cooler (and wetter) summertime conditions CESM2 simulated negative GPP anomalies in these regions. Our analysis cannot diagnose the proximal driver of the GPP anomalies, but given their higher correlation coefficient we assume that summertime temperature anomalies are driving the carbon cycle response, with declines in soil moisture subsequently resulting from higher evapotranspiration fluxes in warmer, more productive years.

The amplification vector also describes a high fraction of the NEP and GPP variability in lower latitudes (Figs. 5-6). The weights from the GPP amplification vectors in mid and low latitudes shows a strong positive correlation with regional peak growing season GPP anomalies in their respective hemispheres (Fig. 7). In contrast to northern high latitudes, weights from GPP amplification vectors in these regions generally show stronger correlations with terrestrial water storage anomalies than they do for air temperature (Fig. 7, Table S2). Thus, in mid and lower latitudes wetter (and cooler) anomalies during the growing season maxima are associated with positive GPP anomalies, whereas drier (and warmer) anomalies are associated with negative GPP anomalies. While seasonal amplification vectors do explain most of the global carbon cycle variability, some regions are better characterized by a seasonal redistribution of carbon fluxes that do not necessarily change the annual carbon flux, just its timing.

The seasonal redistribution of NEP and GPP explains roughly a quarter of global variability in these fluxes (Figs 4-6, S9). This seasonal redistribution of net and gross carbon fluxes is the dominant mode of variability simulated by CESM2-esm in several regions, including temperate forests and agricultural regions in Eastern North America and Europe. The spatial cohesiveness of this pattern is most notable in the northern hemisphere, where the redistribution vector has positive spring GPP anomalies that are associated with warmer-than-average spring temperatures (MAM; Fig. 8). These positive springtime GPP anomalies are subsequently compensated by lower-than-average photosynthesis rates in the summer and fall that tend to be associated with increasing soil moisture stress (JJA and SON; Fig. 8, Table S3). Drier summer and fall conditions could result from higher evapotranspiration in the spring, or also from increased early runoff due to earlier snowmelt during warm springs (Buermann et al., 2013). The ability of CESM2 to replicate the redistribution of NEP and GPP fluxes (Figs 4, 8; Byrne et al. 2020) suggests that the representation of plant phenology and water stress in CESM2 are likely responding in physically and ecologically realistic ways to simulated climate variability. With seasonal redistribution, potential increases in plant productivity from an early green-up that were facilitated by warmer spring temperatures are negated by soil moisture stress later in the growing season, leading to negligible changes in the annual rates of gross and net carbon uptake (mean $\boldsymbol{\theta}$ values close to zero for the redistribution vector; Figs. 5-6).

The regions where a seasonal redistribution vector dominates carbon cycle variability in CESM2-esm (Figs. 4, S9) are also regions where native vegetation in the model use a stress deciduous phenology scheme, or they are under agricultural management, which is explicitly represented by CLM5 in CESM2 (Lawrence et al., 2019; Lombardozzi et al., 2020). Both phenology parameterizations use a growing degree day approach to simulate leaf emergence (or planting date and leaf emergence for the CLM5 crop model), so the strong correlation between air temperature anomalies and SVD weights are expected (Fig. 8, Table S3). We were more surprised, however, by the negative GPP and NEP anomalies that emerge later in the growing season. These seem to be driven by drier- and warmer-than-average conditions that are consistent with satellite observations of vegetation greenness (Buermann et al., 2013; Buermann et al., 2018). Notably, redistribution vectors diagnosed from solar induced fluorescence (SIF) derived GPP in North America are tightly linked with spring (and summer) temperature anomalies (Butterfield et al., 2020; Byrne et al., 2020; Table S1). The larger influence of seasonal

redistribution in temperate latitudes that is simulated in CESM2-esm is also consistent with observations from forests reported in Butterfield et al. (2020), but the overall importance of seasonal redistribution vs. amplification on carbon cycle variability remains uncertain. Indeed, considering the relative importance of these modes of variability may be important in trying to infer appropriate sensitivities and interactions between seasonal to interannual variability in climate, phenology, and ecosystem carbon fluxes from both models and observations.

5. Conclusion

The interannual variability of terrestrial net carbon exchange with the atmosphere in CESM2-esm is low. Accordingly, the model also simulates a weaker-than-observed sensitivity of net carbon exchange to global climate anomalies. This low variability of net carbon fluxes likely results from low interannual variability in photosynthesis anomalies that are simulated by the model, especially in humid tropical forests, and a high covariation gross primary productivity and ecosystem respiration. Our findings emphasize the need to evaluate and revise the parameterization of carbon cycle sensitivity to climate variability, especially in the tropics, that are related to phenology, photosynthetic and stomatal conductance responses to environmental stress, the canopy scaling of these leaf level processes and potential legacy effects from extreme events. The variability in GPP that is simulated by CESM-esm generally shows a latitudinal gradient in climate sensitivities whereby positive NEP and GPP anomalies are driven by warmer and drier conditions in high latitude ecosystems but wetter and cooler conditions across mid and low latitudes.

Our analysis decomposes IAV in terrestrial carbon cycle anomalies into modes of variability that are characterized by seasonal amplification and redistribution of carbon fluxes. Together these modes of variability explain two-thirds of the variability in NEP anomalies and three-quarters of the global variability in GPP. Both CESM and observations show that wetter and cooler springs and summers lead to an amplification signal in GPP, especially over the high latitude ecosystems and temperate and arid regions like western North America. By contrast, the temporal redistribution of GPP anomalies is more strongly associated with variability in springtime temperatures and positive C cycle anomalies that are followed by subsequent soil moisture stress and negative carbon cycle anomalies. This seasonal redistribution of fluxes is the dominant mode of carbon cycle variability in the more mesic temperate ecosystems like the

eastern North America and Europe. The seasonal redistribution of carbon cycle variability is notable because although it is not apparent in more aggregated (annual) measurements of IAV, it does seem widespread in both the model and observations. Thus, while the total magnitude of net and gross terrestrial carbon flux variability simulated by CESM2 may be too low, the simulated interannual and seasonal variability does qualitatively capture patterns of carbon sensitivities to climate variability. More broadly, we contend this kind of analysis is useful in diagnosing strengths and weaknesses in biogeochemical models in comparison to observational data.

Acknowledgments, Samples, and Data

The authors declare no conflicts of interests. The CESM project is supported primarily by the National Science Foundation (NSF). This material is based upon work supported by the National Center for Atmospheric Research, which is a major facility sponsored by the NSF under Cooperative Agreement No. 1852977. Computing and data storage resources, including the Cheyenne supercomputer (doi:10.5065/D6RX99HX), were provided by the Computational and Information Systems Laboratory (CISL) at NCAR. We thank all the scientists, software engineers, and administrators who contributed to the development of CESM2. WRW and DLL were supported by the US Department of Agriculture NIFA Award number 2015-67003-23485. WRW, GKA, and ZB would like to acknowledge support from the NASA Interdisciplinary Science Program award number NNX17AK19G.

Previous and current CESM versions are freely available online (see http://www.cesm.ucar.edu/models/cesm2/release_download.html) with code from https://github.com/ESCOMP/CESM, https://doi.org/10.5065/D67H1H0V). The CESM2-esm-hist data set (doi:10.22033/ESGF/CMIP6.7575) used in this study are also freely available from the Earth System Grid Federation (ESGF; at https://esgf-node.llnl.gov/search/cmip6/, search for CESM2.esm-hist) or from the NCAR Digital Asset Services Hub (DASH; at data.ucar.edu) or from the links provided from the CESM website (at www.cesm.ucar.edu); CESM2 (2019). Code for the analyses presented can be found at WRW's GitHub page (https://github.com/wwieder/CESM2esmIAV/blob/main/esmIAV.ipynb), which has been archived at https://doi.org/10.5281/zenodo.4988114.

Author contribution

WRW conducted the analyses with help from ZB and GKA. WRW wrote the manuscript with contributions from all other authors.

References

Ahlström, A., Raupach, M. R., Schurgers, G., Smith, B., Arneth, A., Jung, M., et al. (2015). The dominant role of semi-arid ecosystems in the trend and variability of the land CO₂ sink. *Science, 348*(6237), 895-899. doi: 10.1126/science.aaa1668.

Alemohammad, S. H., Fang, B., Konings, A. G., Aires, F., Green, J. K., Kolassa, J., et al. (2017). Water, Energy, and Carbon with Artificial Neural Networks (WECANN): A statistically-based estimate of global surface turbulent fluxes and gross primary productivity using solar-induced fluorescence. *Biogeosciences, 14*(18), 4101-4124. doi: 10.5194/bg-14-4101-2017.

Anav, A., Friedlingstein, P., Kidston, M., Bopp, L., Ciais, P., Cox, P., et al. (2013). Evaluating the Land and Ocean Components of the Global Carbon Cycle in the CMIP5 Earth System Models. *Journal of Climate, 26*(18), 6801-6843. doi: 10.1175/jcli-d-12-00417.1.

Anderegg, W. R. L., Ballantyne, A. P., Smith, W. K., Majkut, J., Rabin, S., Beaulieu, C., et al. (2015). Tropical nighttime warming as a dominant driver of variability in the terrestrial carbon sink. *Proceedings of the National Academy of Sciences, 112*(51), 15591-15596. doi: 10.1073/pnas.1521479112.

Arora, V. K., Katavouta, A., Williams, R. G., Jones, C. D., Brovkin, V., Friedlingstein, P., et al. (2020). Carbon–concentration and carbon–climate feedbacks in CMIP6 models and their comparison to CMIP5 models. *Biogeosciences, 17*(16), 4173-4222. doi: 10.5194/bg-17-4173-2020.

Atkin, O. K., Bahar, N. H. A., Bloomfield, K. J., Griffin, K. L., Heskel, M. A., Huntingford, C., et al. (2017). Leaf Respiration in Terrestrial Biosphere Models. In G. Tcherkez & J. Ghashghaie (Eds.), *Plant Respiration: Metabolic Fluxes and Carbon Balance* (pp. 107-142). Cham: Springer International Publishing.

Baldocchi, D., Chu, H., & Reichstein, M. (2018). Inter-annual variability of net and gross ecosystem carbon fluxes: A review. *Agricultural And Forest Meteorology, 249*, 520-533. doi: 10.1016/j.agrformet.2017.05.015.

Baldocchi, D., Falge, E., Gu, L., Olson, R., Hollinger, D., Running, S., et al. (2001). FLUXNET: A New Tool to Study the Temporal and Spatial Variability of Ecosystem–Scale Carbon Dioxide, Water Vapor, and Energy Flux Densities. *Bulletin of the American Meteorological Society, 82*(11), 2415-2434. doi: 10.1175/1520-0477(2001)082<2415:Fantts>2.3.Co;2.

Ballantyne, A. P., Alden, C. B., Miller, J. B., Tans, P. P., & White, J. W. (2012). Increase in observed net carbon dioxide uptake by land and oceans during the past 50 years. *Nature, 488*(7409), 70-72. doi: 10.1038/nature11299.

Ballantyne, A. P., Smith, W., Anderegg, W., Kauppi, P., Sarmiento, J., Tans, P., et al. (2017). Accelerating net terrestrial carbon uptake during the warming hiatus due to reduced respiration. *Nature Climate Change, 7*(2), 148-152. doi: 10.1038/nclimate3204.

Basile, S. J., Lin, X., Wieder, W. R., Hartman, M. D., & Keppel-Aleks, G. (2020). Leveraging the signature of heterotrophic respiration on atmospheric CO2 for model benchmarking. *Biogeosciences*, 17(5), 1293-1308. doi: 10.5194/bg-17-1293-2020.

Bastos, A., Friedlingstein, P., Sitch, S., Chen, C., Mialon, A., Wigneron, J. P., et al. (2018). Impact of the 2015/2016 El Nino on the terrestrial carbon cycle constrained by bottom-up and top-down approaches. *Philos Trans R Soc Lond B Biol Sci, 373*(1760), 20170304. doi: 10.1098/rstb.2017.0304.

Beer, C., Reichstein, M., Tomelleri, E., Ciais, P., Jung, M., Carvalhais, N., et al. (2010). Terrestrial Gross Carbon Dioxide Uptake: Global Distribution and Covariation with Climate. *Science, 329*(5993), 834-838. doi: 10.1126/science.1184984.

Bloom, A. A., Bowman, K. W., Liu, J., Konings, A. G., Worden, J. R., Parazoo, N. C., Meyer, V., Reager, J. T., Worden, H. M., Jiang, Z, Quetin, G. R., Smallman, T. L., Exbrayat, J-F, Yin, Y, Saatchi, S. S., Williams, M., Schimel, D. S. (2020). Lagged effects regulate the inter-annual variability of the tropical carbon balance. *Biogeosciences, 17*(24), 6393-6422. doi:10.5194/bg-17-6393-2020

Bonan, G. B., Davis, K. J., Baldocchi, D., Fitzjarrald, D., & Neumann, H. (1997). Comparison of the NCAR LSM1 land surface model with BOREAS aspen and jack pine tower fluxes. *Journal of Geophysical Research-Atmospheres*, 102(D24), 29065-29075. doi:10.1029/96jd03095

Bonan, G. B., Lombardozzi, D. L., Wieder, W. R., Oleson, K. W., Lawrence, D. M., Hoffman, F. M., & Collier, N. (2019). Model Structure and Climate Data Uncertainty in Historical Simulations of the Terrestrial Carbon Cycle (1850–2014). *Global Biogeochemical Cycles, 33*(10), 1310-1326. doi: 10.1029/2019gb006175.

Bonan, G. B., Oleson, K. W., Fisher, R. A., Lasslop, G., & Reichstein, M. (2012). Reconciling leaf physiological traits and canopy flux data: Use of the TRY and FLUXNET databases in the Community Land Model version 4. *Journal of Geophysical Research: Biogeosciences*, *117*(G2), G02026. doi: 10.1029/2011jg001913.

Bousquet, P., Peylin, P., Ciais, P., Le Quéré, C., Friedlingstein, P., & Tans, P. P. (2000). Regional Changes in Carbon Dioxide Fluxes of Land and Oceans Since 1980. *Science, 290*(5495), 1342-1346. doi: 10.1126/science.290.5495.1342.

Bowman, K. W., Liu, J., Bloom, A. A., Parazoo, N. C., Lee, M., Jiang, Z., et al. (2017). Global and Brazilian Carbon Response to El Niño Modoki 2011–2010. *Earth and Space Science, 4*(10), 637-660. doi: https://doi.org/10.1002/2016EA000204.

Buermann, W., Bikash, P. R., Jung, M., Burn, D. H., & Reichstein, M. (2013). Earlier springs decrease peak summer productivity in North American boreal forests. *Environmental Research Letters, 8*(2), 024027. doi: 10.1088/1748-9326/8/2/024027.

Buermann, W., Forkel, M., O'Sullivan, M., Sitch, S., Friedlingstein, P., Haverd, V., et al. (2018). Widespread seasonal compensation effects of spring warming on northern plant productivity. *Nature, 562*(7725), 110-114. doi: 10.1038/s41586-018-0555-7.

Butterfield, Z., Buermann, W., & Keppel-Aleks, G. (2020). Satellite observations reveal seasonal redistribution of northern ecosystem productivity in response to interannual climate variability. *Remote Sensing Of Environment, 242*, 111755. doi: 10.1016/j.rse.2020.111755.

Byrne, B., Liu, J., Bloom, A. A., Bowman, K. W., Butterfield, Z., Joiner, J., Keenan T.F., Keppel-Aleks G., Parazoo N. C., Yin, Y. (2020). *Contrasting Regional Carbon Cycle Responses to Seasonal Climate Anomalies Across the East-West Divide of Temperate North America. Global Biogeochemical Cycles,* 34(11), e2020GB006598. doi: 10.1029/2020GB006598

Carvalhais, N., Forkel, M., Khomik, M., Bellarby, J., Jung, M., Migliavacca, M., et al. (2014). Global covariation of carbon turnover times with climate in terrestrial ecosystems. *Nature, 514*(7521), 213-217. doi: 10.1038/nature13731.

Cavaleri, M. A., Coble, A. P., Ryan, M. G., Bauerle, W. L., Loescher, H. W., & Oberbauer, S. F. (2017). Tropical rainforest carbon sink declines during El Nino as a result of reduced photosynthesis and increased respiration rates. *The New phytologist, 216*(1), 136-149. doi: 10.1111/nph.14724.

Chen, M., Rafique, R., Asrar, G. R., Bond-Lamberty, B., Ciais, P., Zhao, F., et al. (2017). Regional contribution to variability and trends of global gross primary productivity. *Environmental Research Letters, 12*(10), 105005. doi: 10.1088/1748-9326/aa8978.

Chevallier, F. (2018). Comment on "Contrasting carbon cycle responses of the tropical continents to the 2015-2016 El Nino". *Science, 362*(6418), eaar5432. doi: 10.1126/science.aar5432.

Ciais, P., Yao, Y., Gasser, T., Baccini, A., Wang, Y., Lauerwald, R., Peng, S., Bastos, A., Li, W., Raymond, P. A., Canadell, J. G., Peters, G. P., Andres, R. J., Chang, J., Yue, C., Dolman, A. J.,

Haverd, V., Hartmann, J., Laruelle, G., Konings, A. G., King, A. W., Liu, Y., Luyssaert, S., Maignan, F., Patra, P. K., Peregon, A., Regnier, P., Pongratz, J., Poulter, B., Shvidenko, A., Valentini, R., Wang, R., Broquet, G., Yin, Y., Zscheischler, J., Guenet, B., Goll, D. S., Ballantyne, A.-P., Yang, H., Qiu, C., & Zhu, D. (2020). Empirical estimates of regional carbon budgets imply reduced global soil heterotrophic respiration. *National Science Review, 8*(2). doi: 10.1093/nsr/nwaa145.

Collier, N., Hoffman, F. M., Lawrence, D. M., Keppel-Aleks, G., Koven, C. D., Riley, W. J., et al. (2018). The International Land Model Benchmarking (ILAMB) System: Design, Theory, and Implementation. *Journal of Advances in Modeling Earth Systems, 10*(11), 2731-2754. doi: 10.1029/2018ms001354.

Commane, R., Lindaas, J., Benmergui, J., Luus, K. A., Chang, R. Y., Daube, B. C., et al. (2017). Carbon dioxide sources from Alaska driven by increasing early winter respiration from Arctic tundra. *Proc Natl Acad Sci U S A, 114*(21), 5361-5366. doi:10.1073/pnas.1618567114

Cox, P. M., Pearson, D., Booth, B. B., Friedlingstein, P., Huntingford, C., Jones, C. D., & Luke, C. M. (2013). Sensitivity of tropical carbon to climate change constrained by carbon dioxide variability. *Nature, 494*(7437), 341-344. doi: 10.1038/nature11882.

Danabasoglu, G., Lamarque, J.-F., Bacmeister, J., Bailey, D. A., DuVivier, A. K., Edwards, J., et al. (2020). The Community Earth System Model Version 2 (CESM2). *Journal of Advances in Modeling Earth Systems, 12*(2), e2019MS001916. doi: 10.1029/2019ms001916.

Eyring, V., Bony, S., Meehl, G. A., Senior, C. A., Stevens, B., Stouffer, R. J., & Taylor, K. E. (2016). Overview of the Coupled Model Intercomparison Project Phase 6 (CMIP6) experimental design and organization. *Geosci. Model Dev., 9*(5), 1937-1958. doi: 10.5194/gmd-9-1937-2016.

Fisher, J. B., Sitch, S., Malhi, Y., Fisher, R. A., Huntingford, C., & Tan, S. Y. (2010). Carbon cost of plant nitrogen acquisition: A mechanistic, globally applicable model of plant nitrogen uptake, retranslocation, and fixation. *Global Biogeochemical Cycles, 24*(1), GB1014. doi: 10.1029/2009GB003621.

Fisher, R. A., Wieder, W. R., Sanderson, B. M., Koven, C. D., Oleson, K. W., Xu, C., et al. (2019). Parametric Controls on Vegetation Responses to Biogeochemical Forcing in the CLM5. *Journal of Advances in Modeling Earth Systems, 11*(9), 2879-2895. doi: 10.1029/2019ms001609.

Friedlingstein, P., Jones, M. W., O'Sullivan, M., Andrew, R. M., Hauck, J., Peters, G. P., et al. (2019). Global Carbon Budget 2019. *Earth System Science Data, 11*(4), 1783-1838. doi: 10.5194/essd-11-1783-2019.

Friedlingstein, P., Meinshausen, M., Arora, V. K., Jones, C. D., Anav, A., Liddicoat, S. K., & Knutti, R. (2014). Uncertainties in CMIP5 Climate Projections due to Carbon Cycle Feedbacks. *Journal of Climate, 27*(2), 511-526. doi: 10.1175/jcli-d-12-00579.1.

Fu, Z., Stoy, P. C., Poulter, B., Gerken, T., Zhang, Z., Wakbulcho, G., & Niu, S. (2019). Maximum carbon uptake rate dominates the interannual variability of global net ecosystem exchange. *Global Change Biology, 25*(10), 3381-3394. doi: 10.1111/gcb.14731.

Gaubert, B., Stephens, B. B., Basu, S., Chevallier, F., Deng, F., Kort, E. A., et al. (2019). Global atmospheric CO2 inverse models converging on neutral tropical land exchange, but disagreeing on fossil fuel and atmospheric growth rate. *Biogeosciences, 16*(1), 117-134. doi: 10.5194/bg-16-117-2019.

Golub, G. H., & Reinsch, C. (1971). Singular value decomposition and least squares solutions. In *Linear Algebra* (pp. 134-151): Springer.

Graven, H. D., Keeling, R. F., Piper, S. C., Patra, P. K., Stephens, B. B., Wofsy, S. C., Welp, L. R., Sweeney, C., Tans, P. P., Kelley, J. J., Daube, B. C., Kort, E. A., Santoni, G. W., & Bent, J. D. (2013). Enhanced Seasonal Exchange of CO_2 by Northern Ecosystems Since 1960. *Science*, 341(6150), 1085-1089. doi: 10.1126/science.1239207.

Hoffman, F. M., Randerson, J. T., Arora, V. K., Bao, Q., Cadule, P., Ji, D., et al. (2014). Causes and implications of persistent atmospheric carbon dioxide biases in Earth System Models. *Journal of Geophysical Research-Biogeosciences, 119*(2), 141-162. doi: 10.1002/2013jg002381.

Hu, L., Andrews, A. E., Thoning, K. W., Sweeney, C., Miller, J. B., Michalak, A. M., et al. (2019). Enhanced North American carbon uptake associated with El Nino. *Sci Adv, 5*(6), eaaw0076. doi: 10.1126/sciadv.aaw0076.

Humphrey, V., Zscheischler, J., Ciais, P., Gudmundsson, L., Sitch, S., & Seneviratne, S. I. (2018). Sensitivity of atmospheric CO2 growth rate to observed changes in terrestrial water storage. *Nature, 560*(7720), 628-631. doi: 10.1038/s41586-018-0424-4.

Ito, A., Inatomi, M., Huntzinger, D. N., Schwalm, C., Michalak, A. M., Cook, R., King, A. W., Mao, J., Wei, Y., Post, W. M., Wang, W., Arain, M. A., Huang, S., Hayes, D. J., Ricciuto, D. M., Shi, X., Huang, M., Lei, H., Tian, H., Lu, C., Yang, J., Tao, B., Jain, A., Poulter, B., Peng, S., Ciais, P., Fisher, J. B., Parazoo, N., Schaefer, K., Peng, C., Zeng, N., & Zhao, F. (2016). Decadal trends in the seasonal-cycle amplitude of terrestrial CO2 exchange resulting from the ensemble of terrestrial biosphere models. *Tellus B: Chemical and Physical Meteorology*, 68(1), 28968. doi: 10.3402/tellusb.v68.28968.

Jung, M., Reichstein, M., Margolis, H. A., Cescatti, A., Richardson, A. D., Arain, M. A., et al. (2011). Global patterns of land-atmosphere fluxes of carbon dioxide, latent heat, and sensible heat derived from eddy covariance, satellite, and meteorological observations. *Journal of Geophysical Research, 116*. doi: 10.1029/2010jg001566.

Jung, M., Reichstein, M., Schwalm, C. R., Huntingford, C., Sitch, S., Ahlström, A., et al. (2017). Compensatory water effects link yearly global land CO2 sink changes to temperature. *Nature, 541*(7638), 516-520. doi: 10.1038/nature20780.

Jung, M., Schwalm, C., Migliavacca, M., Walther, S., Camps-Valls, G., Koirala, S., et al. (2020). Scaling carbon fluxes from eddy covariance sites to globe: synthesis and evaluation of the FLUXCOM approach. *Biogeosciences, 17*(5), 1343-1365. doi: 10.5194/bg-17-1343-2020.

Kannenberg, S. A., Bowling, D. R., & Anderegg, W. R. L. (2020). Hot moments in ecosystem fluxes: High GPP anomalies exert outsized influence on the carbon cycle and are differentially driven by moisture availability across biomes. *Environmental Research Letters, 15*(5), 054004. doi: 10.1088/1748-9326/ab7b97.

Keeling, C. D., Whorf, T. P., Wahlen, M., & van der Plichtt, J. (1995). Interannual extremes in the rate of rise of atmospheric carbon dioxide since 1980. *Nature, 375*(6533), 666-670. doi: 10.1038/375666a0.

Kennedy, D., Swenson, S., Oleson, K. W., Lawrence, D. M., Fisher, R., Lola da Costa, A. C., & Gentine, P. (2019). Implementing Plant Hydraulics in the Community Land Model, Version 5. *Journal of Advances in Modeling Earth Systems, 11*(2), 485-513. doi: 10.1029/2018ms001500.

Keppel-Aleks, G., Randerson, J. T., Lindsay, K., Stephens, B. B., Keith Moore, J., Doney, S. C., et al. (2013). Atmospheric Carbon Dioxide Variability in the Community Earth System Model: Evaluation and Transient Dynamics during the Twentieth and Twenty-First Centuries. *Journal of Climate, 26*(13), 4447-4475. doi: 10.1175/jcli-d-12-00589.1.

Keppel-Aleks, G., Wolf, A. S., Mu, M., Doney, S. C., Morton, D. C., Kasibhatla, P. S., et al. (2014). Separating the influence of temperature, drought, and fire on interannual variability in atmospheric CO2. *Global Biogeochemical Cycles, 28*(11), 1295-1310. doi: 10.1002/2014gb004890.

Köhler, P., Frankenberg, C., Magney, T. S., Guanter, L., Joiner, J., & Landgraf, J. (2018). Global Retrievals of Solar- Induced Chlorophyll Fluorescence With TROPOMI: First Results and Intersensor Comparison to OCO- 2. *Geophysical Research Letters, 45*(19), 10,456-410,463. doi: 10.1029/2018gl079031.

Koven, C. D., Hugelius, G., Lawrence, D. M., & Wieder, W. R. (2017). Higher climatological temperature sensitivity of soil carbon in cold than warm climates. *Nature Climate Change, 7*(11), 817-822. doi: 10.1038/nclimate3421.

Lasslop, G., Reichstein, M., Detto, M., Richardson, A. D., & Baldocchi, D. D. (2010). Comment on Vickers et al.: Self-correlation between assimilation and respiration resulting from flux

partitioning of eddy-covariance CO2 fluxes. *Agricultural And Forest Meteorology, 150*(2), 312-314. doi: 10.1016/j.agrformet.2009.11.003.

Lawrence, D. M., Fisher, R. A., Koven, C. D., Oleson, K. W., Swenson, S. C., Bonan, G., et al. (2019). The Community Land Model Version 5: Description of New Features, Benchmarking, and Impact of Forcing Uncertainty. *Journal of Advances in Modeling Earth Systems, 11*(12), 4245-4287. doi: 10.1029/2018ms001583.

Li, X., & Xiao, J. (2019). A Global, 0.05-Degree Product of Solar-Induced Chlorophyll Fluorescence Derived from OCO-2, MODIS, and Reanalysis Data. *Remote Sensing*, 11(5), 517. doi:10.3390/rs11050517

Liddicoat, S. K., Wiltshire, A. J., Jones, C. D., Arora, V. K., Brovkin, V., Cadule, P., Hajima, T., Lawrence, D. M., Pongratz, J., Schwinger, J., Séférian, R., Tjiputra, J. F., & Ziehn, T. (2021). Compatible Fossil Fuel CO2 Emissions in the CMIP6 Earth System Models' Historical and Shared Socioeconomic Pathway Experiments of the Twenty-First Century. *Journal of Climate*, 34(8), 2853-2875. doi: 10.1175/jcli-d-19-0991.1.

Lindsay, K. (2017). A Newton–Krylov solver for fast spin-up of online ocean tracers. *Ocean Modelling, 109*, 33-43. doi: 10.1016/j.ocemod.2016.12.001.

Lindsay, K., Bonan, G. B., Doney, S. C., Hoffman, F. M., Lawrence, D. M., Long, M. C., Mahowald, N. M., Keith Moore, J., Randerson, J. T., & Thornton, P. E. (2014). Preindustrial-Control and Twentieth-Century Carbon Cycle Experiments with the Earth System Model CESM1(BGC). *Journal of Climate*, 27(24), 8981-9005. doi: 10.1175/jcli-d-12-00565.1.

Liu, J., Bowman, K. W., Schimel, D. S., Parazoo, N. C., Jiang, Z., Lee, M., et al. (2017). Contrasting carbon cycle responses of the tropical continents to the 2015-2016 El Nino. *Science, 358*(6360), eaam5690. doi: 10.1126/science.aam5690.

Lombardozzi, D. L., Lu, Y., Lawrence, P. J., Lawrence, D. M., Swenson, S., Oleson, K. W., et al. (2020). Simulating Agriculture in the Community Land Model Version 5. *Journal of Geophysical Research: Biogeosciences, 125*(8), e2019JG005529. doi: 10.1029/2019jg005529.

Martínez-Vilalta, J., Sala, A., Asensio, D., Galiano, L., Hoch, G., Palacio, S., Piper, F. I., & Lloret, F. (2016). Dynamics of non-structural carbohydrates in terrestrial plants: a global synthesis. *Ecological Monographs*, 86(4), 495-516. doi: 10.1002/ecm.1231.

Meehl, G. A., Shields, C., Arblaster, J. M., Annamalai, H., & Neale, R. (2020). Intraseasonal, Seasonal, and Interannual Characteristics of Regional Monsoon Simulations in CESM2. *Journal of Advances in Modeling Earth Systems, 12*(6), e2019MS001962. doi: 10.1029/2019ms001962.

Melaas, E. K., Richardson, A. D., Friedl, M. A., Dragoni, D., Gough, C. M., Herbst, M., et al. (2013). Using FLUXNET data to improve models of springtime vegetation activity onset in forest ecosystems. *Agricultural And Forest Meteorology, 171-172*, 46-56. doi: 10.1016/j.agrformet.2012.11.018.

O'Sullivan, M., Smith, W. K., Sitch, S., Friedlingstein, P., Arora, V. K., Haverd, V., et al. (2020). Climate- driven variability and trends in plant productivity over recent decades based on three global products. *Global Biogeochemical Cycles, n/a*(n/a), e2020GB006613. doi: 10.1029/2020gb006613.

Pastorello, G., Papale, D., Chu, H., Trotta, C., Agarwal, D., Canfora, E., et al. (2017). A New Data Set to Keep a Sharper Eye on Land-Air Exchanges. *EOS, 98*. doi: 10.1029/2017eo071597.

Piao, S., Liu, Z., Wang, Y., Ciais, P., Yao, Y., Peng, S., Chevallier, F., Friedlingstein, P., Janssens, I. A., Penuelas, J., Sitch, S., & Wang, T. (2018). On the causes of trends in the seasonal amplitude of atmospheric CO_2. *Glob Chang Biol*, 24(2), 608-616. doi: 10.1111/gcb.13909.

Piao, S., Wang, X., Wang, K., Li, X., Bastos, A., Canadell, J. G., et al. (2020). Interannual variation of terrestrial carbon cycle: Issues and perspectives. *Glob Chang Biol, 26*(1), 300-318. doi: 10.1111/gcb.14884.

Poulter, B., Frank, D., Ciais, P., Myneni, R. B., Andela, N., Bi, J., et al. (2014). Contribution of semi-arid ecosystems to interannual variability of the global carbon cycle. *Nature, 509*(7502), 600-603. doi: 10.1038/nature13376.

Raczka, B. M., Davis, K. J., Huntzinger, D., Neilson, R. P., Poulter, B., Richardson, A. D., et al. (2013). Evaluation of continental carbon cycle simulations with North American flux tower observations. *Ecological Monographs, 83*(4), 531-556. doi: 10.1890/12-0893.1.

Randerson, J. T., Chapin, F. S., Harden, J. W., Neff, J. C., & Harmon, M. E. (2002). Net ecosystem production: A comprehensive measure of net carbon accumulation by ecosystems. *Ecological Applications*, 12(4), 937-947. doi:10.1890/1051-0761(2002)012[0937:Nepacm]2.0.Co;2

Rödenbeck, C., Zaehle, S., Keeling, R., & Heimann, M. (2018a). History of El Nino impacts on the global carbon cycle 1957-2017: a quantification from atmospheric CO2 data. *Philos Trans R Soc Lond B Biol Sci, 373*(1760), 20170303. doi: 10.1098/rstb.2017.0303.

Rödenbeck, C., Zaehle, S., Keeling, R., & Heimann, M. (2018b). How does the terrestrial carbon exchange respond to inter-annual climatic variations? A quantification based on atmospheric CO2 data. *Biogeosciences, 15*(8), 2481-2498. doi: 10.5194/bg-15-2481-2018.

Running, S. W., Nemani, R. R., Heinsch, F. A., Zhao, M., Reeves, M., & Hashimoto, H. (2004). A Continuous Satellite-Derived Measure of Global Terrestrial Primary Production. *BioScience, 54*(6), 547-560. doi: 10.1641/0006-3568(2004)054[0547:Acsmog]2.0.Co;2.

Schimel, D., Pavlick, R., Fisher, J. B., Asner, G. P., Saatchi, S., Townsend, P., et al. (2015). Observing terrestrial ecosystems and the carbon cycle from space. *Global Change Biology, 21*(5), 1762-1776. doi: 10.1111/gcb.12822.

Schimel, D., Stephens, B. B., & Fisher, J. B. (2015). Effect of increasing CO_2 on the terrestrial carbon cycle. *Proceedings of the National Academy of Sciences*, 112(2), 436-441. doi: 10.1073/pnas.1407302112.

Schwalm, C. R., Williams, C. A., Schaefer, K., Arneth, A., Bonal, D., Buchmann, N., et al. (2010). Assimilation exceeds respiration sensitivity to drought: A FLUXNET synthesis. *Global Change Biology, 16*(2), 657-670. doi: 10.1111/j.1365-2486.2009.01991.x.

Shi, M., Fisher, J. B., Brzostek, E. R., & Phillips, R. P. (2016). Carbon cost of plant nitrogen acquisition: global carbon cycle impact from an improved plant nitrogen cycle in the Community Land Model. *Global Change Biology, 22*(3), 1299-1314. doi: 10.1111/gcb.13131.

Tagesson, T., Schurgers, G., Horion, S., Ciais, P., Tian, F., Brandt, M., et al. (2020). Recent divergence in the contributions of tropical and boreal forests to the terrestrial carbon sink. *Nature Ecology & Evolution, 4*(2), 202-209. doi: 10.1038/s41559-019-1090-0.

Trumbore, S. (2006). Carbon respired by terrestrial ecosystems - recent progress and challenges. *Global Change Biology, 12*(2), 141-153. doi: 10.1111/j.1365-2486.2006.01067.x.

Welp, L. R., Randerson, J. T., & Liu, H. P. (2007). The sensitivity of carbon fluxes to spring warming and summer drought depends on plant functional type in boreal forest ecosystems. *Agricultural and Forest Meteorology, 147*(3-4), 172-185. doi: 10.1016/j.agrformet.2007.07.010

Wang, W., Ciais, P., Nemani, R. R., Canadell, J. G., Piao, S., Sitch, S., et al. (2013). Variations in atmospheric CO2 growth rates coupled with tropical temperature. *Proc Natl Acad Sci U S A, 110*(32), 13061-13066. doi: 10.1073/pnas.1219683110.

Wieder, W. R., Lawrence, D. M., Fisher, R. A., Bonan, G. B., Cheng, S. J., Goodale, C. L., et al. (2019). Beyond Static Benchmarking: Using Experimental Manipulations to Evaluate Land Model Assumptions. *Global Biogeochem Cycles, 33*(10), 1289-1309. doi: 10.1029/2018GB006141.

Wozniak, M. C., Bonan, G. B., Keppel-Aleks, G., & Steiner, A. L. (2020). Influence of Vertical Heterogeneities in the Canopy Microenvironment on Interannual Variability of Carbon Uptake in Temperate Deciduous Forests. *Journal of Geophysical Research: Biogeosciences, 125*(8), e2020JG005658. doi: 10.1029/2020jg005658.

Zeng, N., Mariotti, A., & Wetzel, P. (2005). Terrestrial mechanisms of interannual CO2 variability. *Global Biogeochemical Cycles, 19*(1). doi: 10.1029/2004gb002273.

Zhang, X., Gurney, K. R., Peylin, P., Chevallier, F., Law, R. M., Patra, P. K., et al. (2013). On the variation of regional CO2 exchange over temperate and boreal North America. *Global Biogeochemical Cycles, 27*(4), 991-1000. doi: 10.1002/gbc.20091.

Zhang, Y., Joiner, J., Gentine, P., & Zhou, S. (2018). Reduced solar-induced chlorophyll fluorescence from GOME-2 during Amazon drought caused by dataset artifacts. *Global Change Biology, 24*(6), 2229-2230. doi: 10.1111/gcb.14134.

Zscheischler, J., Fatichi, S., Wolf, S., Blanken, P. D., Bohrer, G., Clark, K., Desai, A. R., Hollinger, D., Keenan, T., Novick, K. A., & Seneviratne, S. I. (2016). Short-term favorable weather conditions are an important control of interannual variability in carbon and water fluxes. *J Geophys Res Biogeosci*, 121(8), 2186-2198. doi: 10.1002/2016JG003503.

Zscheischler, J., Mahecha, M. D., von Buttlar, J., Harmeling, S., Jung, M., Rammig, A.et al. (2014). A few extreme events dominate global interannual variability in gross primary production. *Environmental Research Letters*, 9(3), 035001. doi: 10.1088/1748-9326/9/3/035001

Figure captions

Figure 1. Detrended annual anomalies of global carbon fluxes, climate drivers, and their correlation. Upper panels show: (a) Atmospheric CO_2 growth rate reported by the global carbon project (Friedlingstein et al., 2019) and net ecosystem production (NEP) simulated CESM2-esm (green and black lines, respectively); (b) NEP, terrestrial water storage (TWS), and tropical air temperature anomalies simulated by CESM2-esm (black, blue, and red lines respectively. Lower panels show correlations between simulated: (c) TWS, which is positively correlated to simulated NEP anomalies; and (d) Tropical air temperature, which is negatively correlated to simulated NEP anomalies. Note, for convenience we inverted the sign of the atmospheric growth rate in (a) so that positive anomalies in C fluxes show net land C uptake for both the model and observations.

Figure 2. Correlations of grid cell carbon fluxes simulated by CESM2-esm from 1960-2015: (a) Variance in NEP versus GPP and R_{eco} (shown in black and green, respectively); and (b) Correlation of anomalies in R_{eco} and GPP. Pearson correlation coefficients and regression slopes from each relationship are provided in each panel, all correlations are significant ($p < 0.001$).

Figure 3. Correlation coefficients between detrended annual anomalies that are simulated by CESM2-esm from 1960-2014. Panels show the correlation between NEP and (a) terrestrial water storage, (b) air temperature, (c) GPP, and (d) R_{eco}. Only statistically significant correlations ($p < 0.05$, when $|r| > 0.226$ for 55 years of data) are shown.

Figure 4. Fraction of variance in detrended NEP anomalies that was explained by (a) seasonal amplification or (b) seasonal redistribution vectors. Globally, these two vectors explained 39% and 29% of the variance in monthly NEP anomalies, respectively.

Figure 5. Zonal mean climatology of monthly NEP and singular vectors associated with seasonal amplification and temporal redistribution of NEP (grey, blue, and red lines respectively) for the northern hemisphere and southern hemisphere (top and bottom rows, respectively). Panels show: (a) high latitude ecosystems, 50-80°N; (b, d) northern and southern temperate mid latitudes, 20-50°N and 20-50°S; and the (c, e) tropics, 0-20°N and 0-20°S, respectively. The magnitude of the singular vectors is arbitrary (y-axis). Mean fraction of variance explained and θ values, which indicate the net impact on the integrated seasonal signal of NEP for each singular vector, are also provided. Note x-axis was shifted for southern hemisphere plots to show the climatology for austral summer.

Figure 6. Zonal mean climatology of monthly GPP and singular vectors associated with seasonal amplification and temporal redistribution of GPP (grey, blue, and red lines respectively) for the northern hemisphere and southern hemisphere (top and bottom rows, respectively). Panels organized as in Fig. 5. Note x-axis was shifted for southern hemisphere plots to show the climatology for austral summer.

Figure 7. Pearson correlation coefficients between SVD weights from the amplification vector with seasonal anomalies of GPP, terrestrial water storage (TWS), and air temperature (TBOT) simulated by CESM2-esm from 1960-2014. Only statistically significant ($p < 0.05$) correlations are shown ($|r| > 0.26$, two-tailed test, $n = 55$).

Figure 8. Pearson correlation coefficients between SVD weights from the redistribution vector with seasonal anomalies of GPP, terrestrial water storage (TWS), and air temperature (TBOT) simulated by CESM2-esm from 1960-2014. Only statistically significant ($p < 0.05$) correlations are shown ($|r| > 0.26$, two-tailed test, $n = 55$).

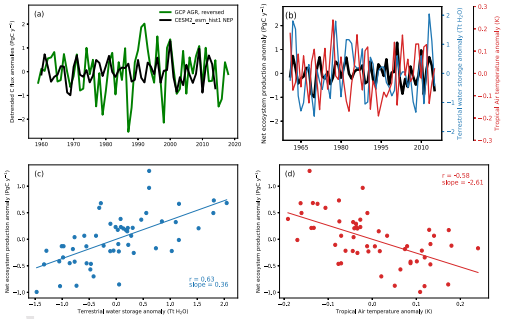

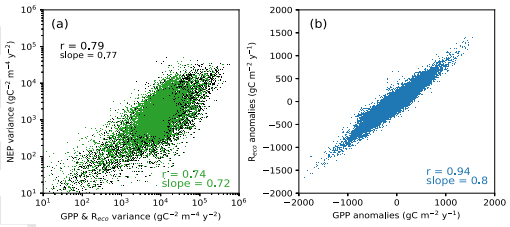

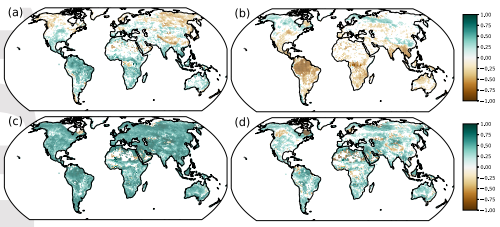

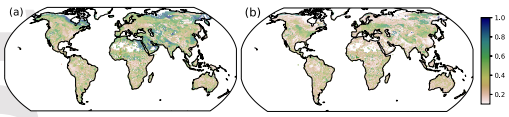

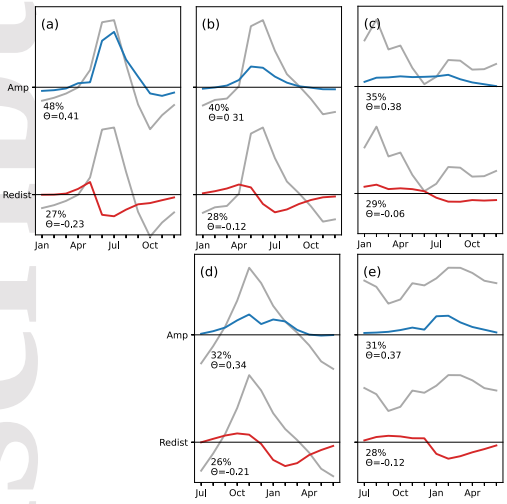

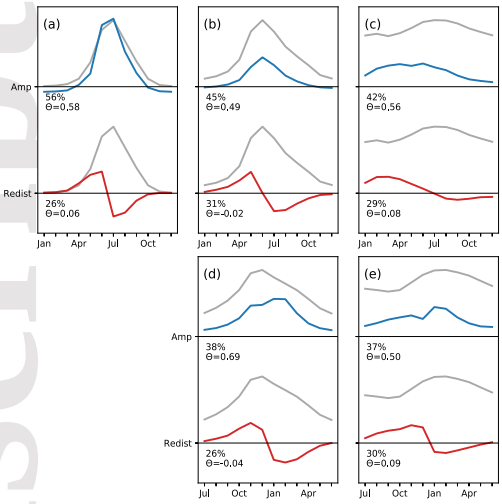

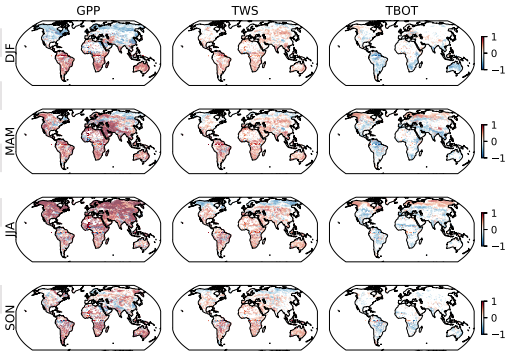

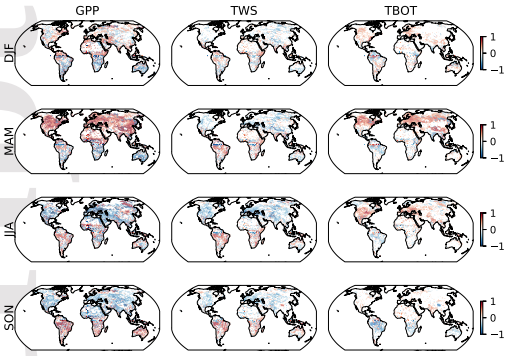

Global Biogeochemical Cycles

Supporting Information for

Interannual and seasonal drivers of carbon cycle variability represented by the Community Earth System Model (CESM2)

William R. Wieder[1,2], Zachary Butterfield[3], Keith Lindsay[1], Danica L. Lombardozzi[1], Gretchen Keppel-Aleks[3]

[1] Climate and Global Dynamics Laboratory, National Center for Atmospheric Research, Boulder, CO 80307, USA.

[2] Institute of Arctic and Alpine Research, University of Colorado, Boulder, CO 80309, USA

[3] Department of Climate and Space Sciences and Engineering, University of Michigan, Ann Arbor, MI, 48109, USA

Contents of this file

Introduction

Supporting information that includes additional figures and tables that describe the statistical methods applied and results from the simulations presented in the paper.

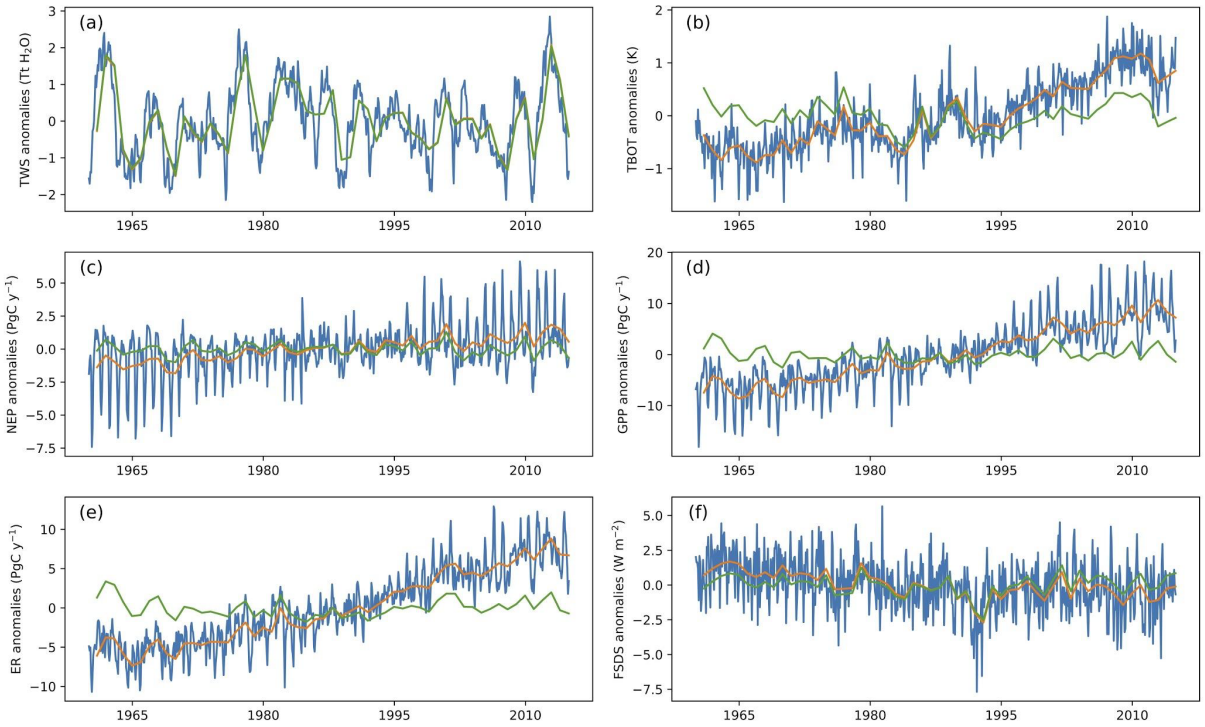

Figure S1. Global monthly anomalies, annual anomalies, and detrended annual anomalies (blue, orange and green lines respectively). Panels show variability in globally summed: (a) terrestrial water storage (TWS); (b) Air temperature (TBOT); (c) Net ecosystem production (NEP); (d) Gross primary productivity (GPP), (e) Ecosystem respiration (ER); and (f) incoming solar radiation (FSDS simulated by CESM-esm over vegetated terrestrial grid cells over the end of the historical period (1960-2014).

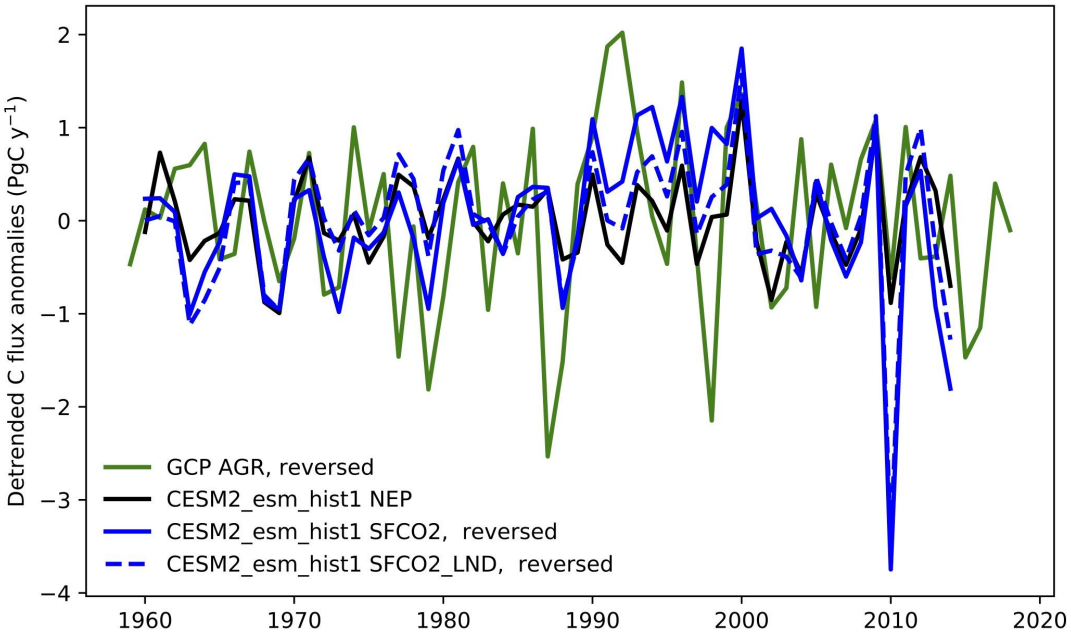

Figure S2. Detrended annual anomalies of global carbon fluxes showing the dominance of terrestrial carbon fluxes of the total IAV of net carbon fluxes simulated by CESM. As in Fig. 1, we show the atmospheric CO_2 growth rate reported by the global carbon project (green line; Friedlingstein et al. 2019), net ecosystem production (NEP) simulated CESM2-ESM (black line), the IAV of the total CESM2 surface CO_2 flux (solid blue line), and the IAV of surface CO_2 flux from terrestrial ecosystems (dashed blue line). Differences between the total surface and land CO_2 fluxes (solid and dashed blue lines) show the influence of IAV in ocean fluxes simulated by CESM2. Differences between land CO_2 flux and NEP show the effect of fire and land use change on terrestrial carbon fluxes. Note, for convenience we inverted the sign of the atmospheric growth rate and surface CO_2 fluxes (green and blue lines) so that positive anomalies show net land C uptake for all fluxes.

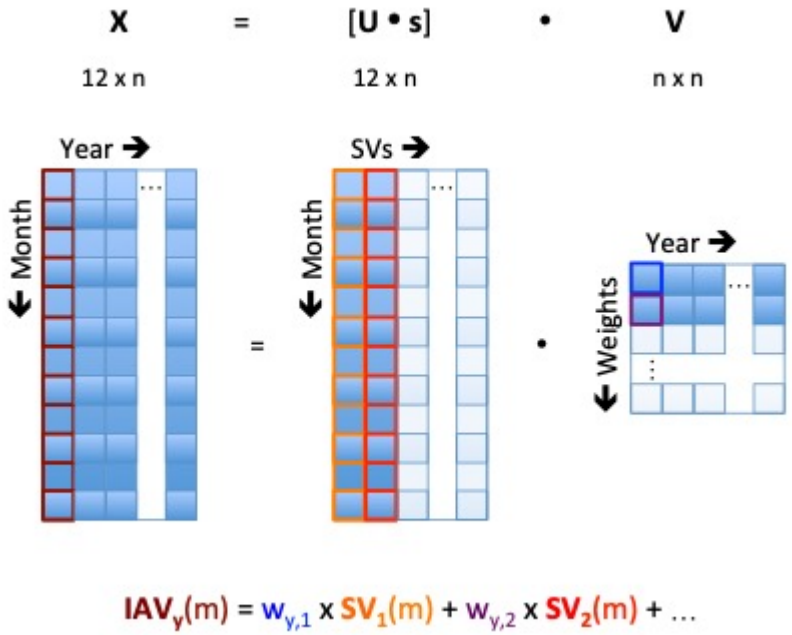

Figure S3. To decompose the annual cycle of detrended GPP time series simulated in each terrestrial grid cell, we used a singular value decomposition method (SVD; Golub and Reinsch 1971; see also Butterfield et al. 2020). The SVD method applied to a 12 x 55 matrix (12 months by 55 years included in our analysis) of annual GPP anomalies (IAV_y) resulted in three matrices, U, s, and V, the middle of which is a 55 x 55 diagonal matrix. The product of U and s provided a matrix of singular vectors (SV_i), the elements of which reflect the month (m) of year (y), that represent common seasonal patterns or modes within the data. The matrix V contained weights (wy,i) that quantify how prominent a singular vector was for any given year. Thus, the simulated IAV time series for a grid cell in any given year could be fully reconstructed as a weighted sum of singular vectors. The singular vectors are ranked by the fraction of variance they explain in the GPP time series, and the first two describe the majority (~75%) of GPP variability. Thus, we focused our analysis on only these first two singular vectors.

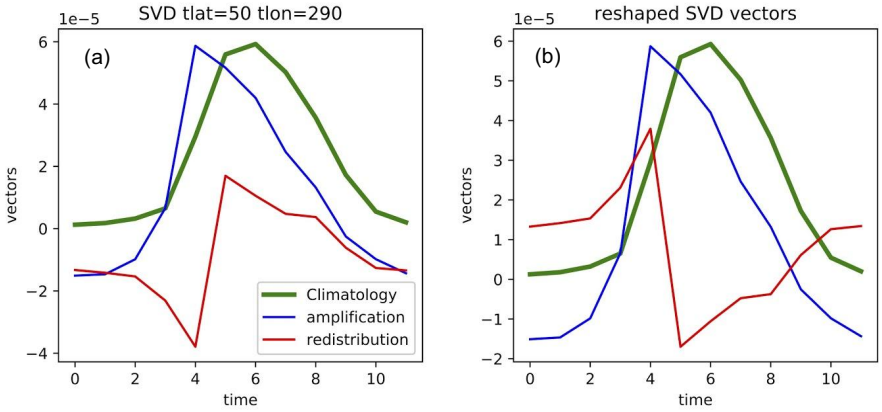

Figure S4. Example grid cell (50°N, 70°W) showing the monthly climatology of GPP fluxes (green) and SVD vectors identified as amplification and redistribution vectors (blue and red, respectively). The amplification vector was identified by its higher correlation with the monthly climatology of GPP fluxes (a). For this grid cell, the redistribution vector (as well as the associated values for weights and theta) was reversed (b), so that positive springtime anomalies occurred before the negative summer anomalies.

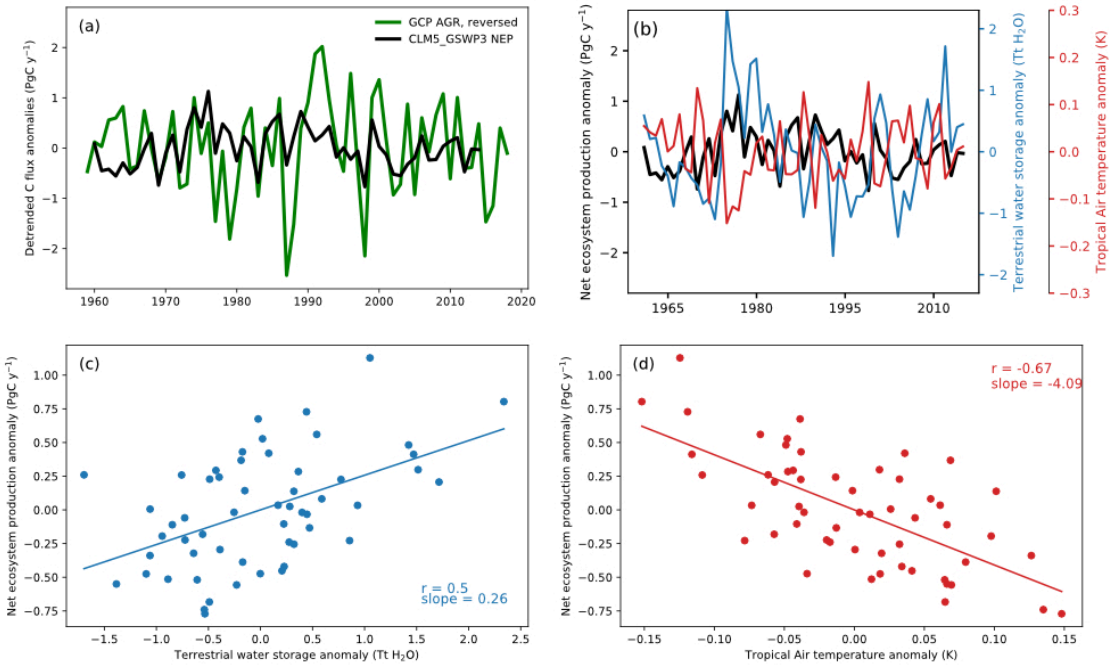

Figure S5. Detrended annual anomalies of global carbon fluxes showing low IAV for net carbon fluxes simulated by offline CLM5 simulations forced with GSWP3 climate reanalysis data through 2014 (see Lawrence et al. 2019). As in Figures 1 and S2, we show the atmospheric CO_2 growth rate reported by the Global Carbon Project, diagnosed from net biome production simulated by an ensemble of land models (green line; Friedlingstein et al. 2019), net ecosystem production (NEP) simulated CLM5 (black line). Although the model captures the sign of terrestrial carbon cycle IAV observed in the atmospheric record, it does not simulate the appropriate magnitude of response to the 1986-87 or 1997-98 El Niño events. Note, for convenience we inverted the sign of the atmospheric growth rate (green line) so that positive anomalies show net land C uptake for all fluxes.

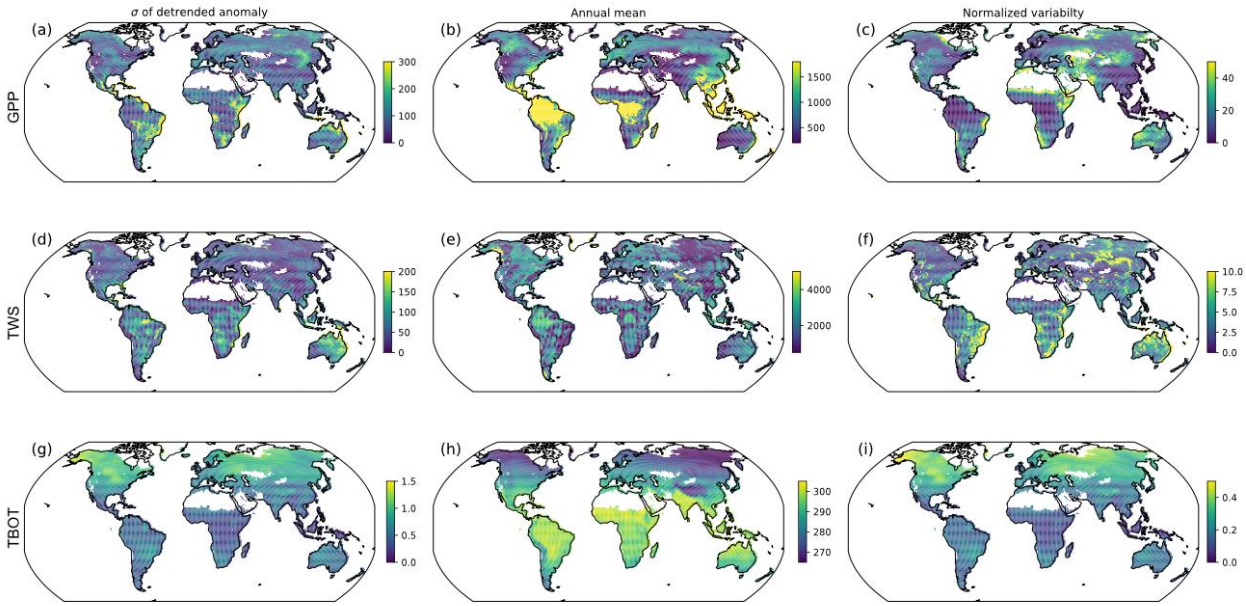

Figure S6. Characterization of GPP (top row), terrestrial water storage (TWS, middle row), and air temperature (TBOT, bottom row) simulated by CESM2-ESM. The first column (a, d, g) shows the standard deviation of detrended annual anomalies (units: gC m^{-2} y^{-1}, kg H_2O m^{-2}, and K, respectively) The second column (b, e, h) shows the annual mean simulated between 1960-2014 (units: gC m^{-2} y^{-1}, kg H_2O m^{-2}, and K, respectively). The third column (c, f, i) shows coefficient of variation (the units %, calculated and the quotient of first and second columns × 100).

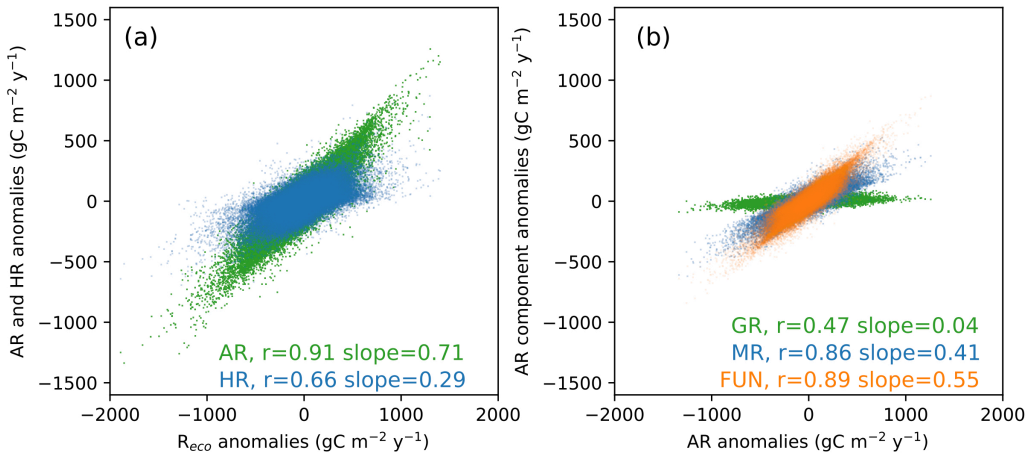

Figure S7. Gridcell correlations of annual (a) R_{eco} anomalies with anomalies of component fluxes autotrophic and heterotrophic respiration (AR and HR, respectively). Panel (b) AR anomalies with anomalies of component fluxes: growth respiration, maintenance respiration, and from the fixation and uptake of nitrogen module (GR, MR, and FUN, respectively). Correlation coefficients and slopes show that R_{eco} anomalies are most strongly correlated with AR anomalies, which are most strongly linked to the fluxes calculated by the FUN module in CESM2-esm.

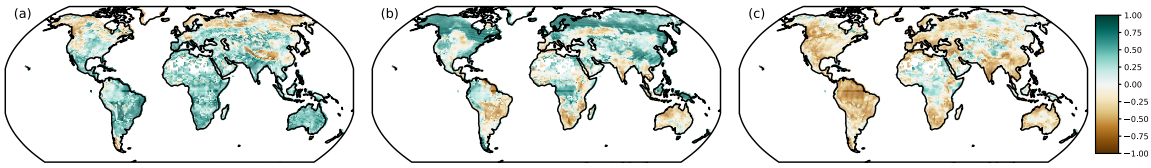

Figure S8. Correlation coefficients between detrended annual anomalies that are simulated by CESM2-esm from 1960-2014. Panels show the correlation between (a) GPP and terrestrial water storage; (b) GPP and air temperature; and (c) terrestrial water storage and air temperature. Only statistically significant correlations ($p < 0.05$, when $|r| > 0.226$ for 55 years of data) are shown.

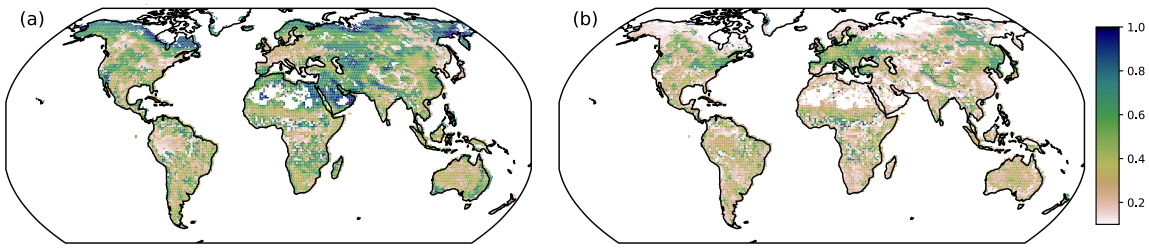

Figure S9. Fraction of variance in detrended GPP anomalies that was explained by (a) seasonal amplification or (b) seasonal redistribution vectors, as in Figure 4. Globally, these two vectors explained 45% and 29% of the variance in monthly GPP anomalies, respectively.

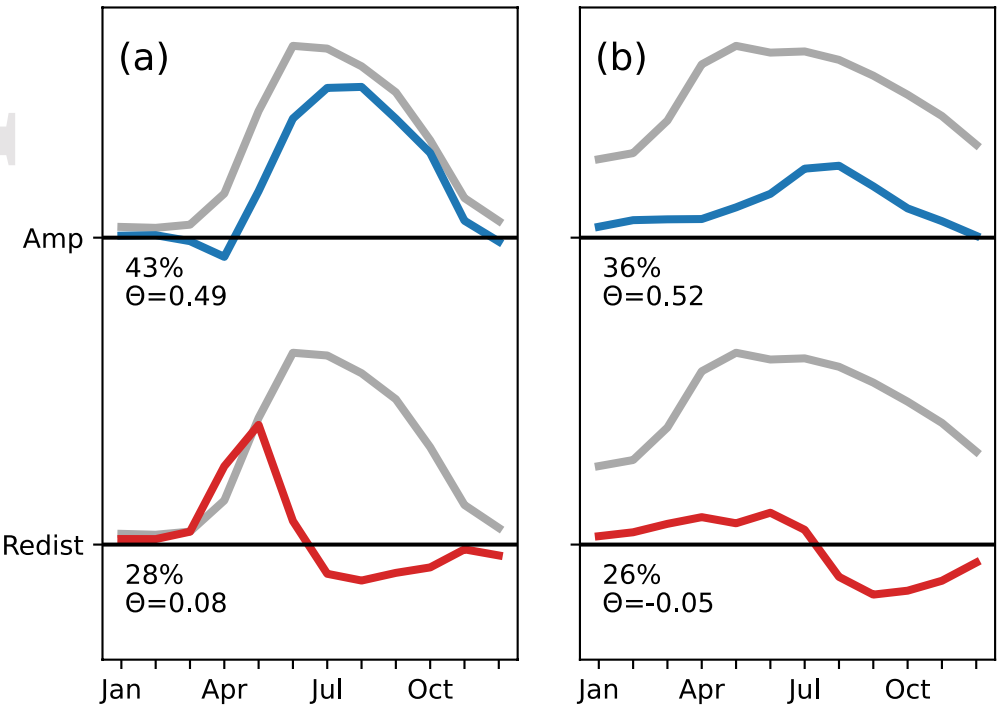

Figure S10. Zonal mean climatology of monthly heterotrophic respiration (HR) and singular vectors associated with seasonal amplification and temporal redistribution of HR (grey, blue, and red lines respectively) for the northern hemisphere. As in Figs 5-6, panels show: (a) high latitude ecosystems, 50-80°N; (b, d) northern temperate mid latitudes, 20-50°N. The magnitude of the singular vectors is arbitrary (y-axis). Mean fraction of variance explained and θ values, which indicate the net impact on the integrated seasonal signal of HR for each singular vector, are also provided.

Table S1. Coefficients of variability in four North American ecoregions defined in Butterfield et al (2020): Temperate Mixed Forest (TMF, 43°–48° N, 84°–94° W), Boreal Coniferous Forest (BCF, 54°–59° N, 94°–104° W), Midwest Cropland (MC, 39°–44° N, 86°–96° W), and Canadian Great Plains (CGP, 50°–55° N, 105°–115° W). To compare with remote sensing variability estimates reported in Butterfield et al. (2020) we define the coefficient of variability as the ratio of the interannual standard deviations to the seasonal amplitude of the multi-year mean. Both model and remote sensing results use nine years of data, 2006-2014 for the model and 2007-2015 for the remote sensing. All values are reported in %.

Region	CESM2	GOME-2 SIF	MODIS NIRv	MODIS NDVI	AVHRR NDVI
TMF	5.2	2.3	1.6	2.2	3.2
BCF	2.4	4.1	2.5	1.9	2.9
MC	1.4	1.8	2.6	2.0	1.5
CGP	2.6	2.8	3.1	2.2	2.5

Table S2. Mean Pearson's correlation coefficients between SVD weights from the amplification vectors and seasonal anomalies in GPP, terrestrial water storage, and air temperature (Fig. 7) for regions. As in Fig. 6, regions here include high-latitude ecosystems, 50-80°N; northern temperate mid-latitudes, 20-50°N, tropics, 0-20°N and 0-20°S, respectively; and southern temperate mid-latitudes, 20-50°S.

	GPP				Terrestrial Water Storage				Air temperature			
Region	**DJF**	**MAM**	**JJA**	**SON**	**DJF**	**MAM**	**JJA**	**SON**	**DJF**	**MAM**	**JJA**	**SON**
NH high	-0.45	0.22	0.95	0.41	-0.05	-0.17	-0.34	-0.21	0.21	0.38	0.38	0.13
NH mid	-0.11	0.70	0.76	0.15	0.38	0.45	0.44	0.34	-0.03	-0.26	-0.30	-0.10
NH tropics	0.50	0.67	0.67	0.45	0.54	0.59	0.50	0.40	-0.24	-0.44	-0.42	-0.27
SH tropics	0.58	0.59	0.59	0.70	0.46	0.54	0.56	0.58	-0.31	-0.32	-0.15	-0.32
SH mid	0.68	0.59	0.42	0.69	0.49	0.51	0.51	0.48	-0.38	-0.28	-0.28	-0.26

Table S3. Mean Pearson's correlation coefficients between SVD weights from the redistribution vectors and seasonal anomalies in GPP, terrestrial water storage, and air temperature (Fig. 8) for regions. As in Fig. 6, regions here include high-latitude ecosystems, 50-80°N; northern temperate mid-latitudes, 20-50°N, tropics, 0-20°N and 0-20°S, respectively; and southern temperate mid-latitudes, 20-50°S.

	GPP				Terrestrial Water Storage				Air Temperature			
Region	**DJF**	**MAM**	**JJA**	**SON**	**DJF**	**MAM**	**JJA**	**SON**	**DJF**	**MAM**	**JJA**	**SON**
NH high	-0.05	0.46	-0.11	-0.40	-0.18	-0.16	-0.24	-0.25	0.30	0.30	0.22	0.04
NH mid	0.15	0.47	-0.33	-0.41	-0.17	-0.22	-0.40	-0.32	0.33	0.31	0.33	0.21
NH tropics	0.38	0.43	0.10	-0.11	0.29	0.31	0.24	0.15	-0.13	-0.25	-0.16	-0.08
SH tropics	-0.06	0.03	0.31	0.42	0.12	0.20	0.29	0.38	-0.01	-0.13	-0.06	-0.26
SH mid	-0.30	-0.30	0.13	0.28	-0.13	-0.01	0.08	0.10	0.07	-0.01	-0.11	-0.22